# Amorphous Silicon Based Solar Cells

Xunming Deng and Eric A. Schiff

# Table of Contents

1 Overview 3
1.1 Amorphous Silicon: The First Bipolar Amorphous Semiconductor 3
1.2 Designs for Amorphous Silicon Solar Cells: A Guided Tour 6
pin Photodiodes 6
Substrate and Superstrate Designs 7
Multijunction Solar Cells 8
1.3 Staebler-Wronski Effect 8
1.4 Synopsis of this Chapter 9
2 Atomic and Electronic Structure of Hydrogenated Amorphous Silicon 11
2.1 Atomic Structure 11
2.2 Defects and Metastability 12
2.3 Electronic Density-of-States 13
2.4 Bandtails, Bandedges, and Bandgaps 13
2.5 Defects & Gap States 15
2.6 Doping 15
2.7 Alloying & Optical Properties 16
Section 3 Depositing Amorphous Silicon 18
3.1 Survey of Deposition Techniques 18
3.2 RF Glow Discharge Deposition 18
3.3 Glow Discharge Deposition at different frequencies 21
VHF Glow Discharge Deposition 22
Microwave Glow Discharge Deposition 23
3.4 Hot-wire Chemical Vapor Deposition 23
3.5 Other Deposition Methods 24
3.6 Hydrogen Dilution 24
3.7 Alloys & Doping 25
4 Understanding a-Si *pin* cells 27
4.1 Electronic structure of a pin device 27
4.2 Photocarrier drift in absorber layers 28
4.3 Absorber Layer Design of a pin solar cell 30
4.4 The Open-Circuit Voltage 32
4.5 Optical design of a-Si:H Solar Cells 34
4.6 Cells under Solar Illumination 37
Section 5 Multiple Junction Solar Cells 40
5.1 Advantages of multiple junction solar cells 40
5.2 Using Alloys for cells with different bandgaps 41
Bandgap Grading 43
a-SiC alloys 43
5.3 a-Si/a-SiGe tandem and a-Si/a-SiGe/a-SiGe triple junction solar cells 44
Current matching 45
Tunnel junctions 45

IV Measurement 46
Quantum Efficiency Measurements in Multijunction Cells 46
Matching Component Cells in Multijunction Designs 47
High efficiency multiple-junction solar cells 48
5.4 Microcrystalline Silicon Solar Cells 48
5.5 Micromorph and other μc-Si based multijunction cells 49
Section 6 Modules Manufacturing 50
Continuous Roll-to-Roll Manufacturing on SS substrate 50
6.2 a-Si module production on glass superstrate 52
6.3 Manufacturing Cost, Safety and Other Issues 53
6.4 Module performances 53
Section 7 Conclusions and Future Projections 55
7.1 Status and Competitiveness of a-Si Photovoltaics 55
7.2 Critical Issues for Further Enhancement and Future Potential 55
Acknowledgments 57

# 1 Overview

## *1.1 Amorphous Silicon: The First Bipolar Amorphous Semiconductor*

Crystalline semiconductors are very well known, including silicon (the basis of the integrated circuits used in modern electronics), Ge (the material of the first transistor), GaAs and the other III-V compounds (the basis for many light emitters), and CdS (often used as a light sensor). In crystals, the atoms are arranged in near-perfect, regular arrays or *lattices*. Of course the lattice must be consistent with the underlying chemical bonding properties of the atoms. For example, a silicon atom forms four covalent bonds to neighboring atoms arranged symmetrically about it. This "tetrahedral" configuration is perfectly maintained in the "diamond" lattice of crystal silicon.

There are also many *non-crystalline* semiconductors. In these materials the chemical bonding of atoms is nearly unchanged from crystals. Nonetheless, a fairly small, disorderly variation in the angles between bonds eliminates the regular lattice structure. Such non-crystalline semiconductors can have fairly good electronic properties – sufficient for many applications. The first commercially important example was xerography [1,2], which exploited the *photoconductivity* of non-crystalline selenium. As do all semiconductors, selenium absorbs those photons from an incident light beam that have photon energies exceeding some threshold energy. The photon that is absorbed generates a positively-charged "hole" and a negatively charged electron that are separated and swept away by the large electric fields used in xerography.

However, solar cells require that photogenerated electrons and holes be separated by

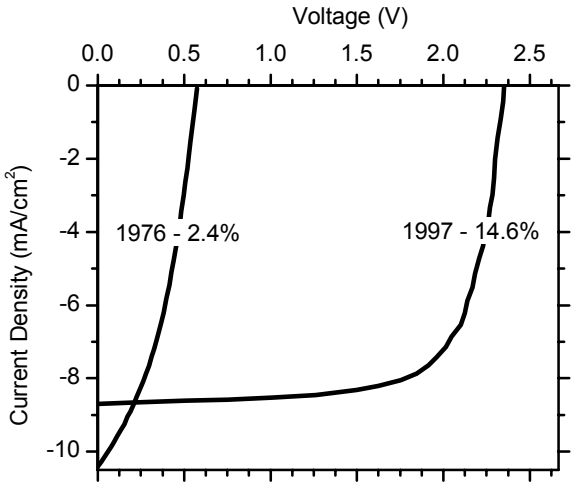


FIG. 1: Current density vs. voltage under solar illumination for a very early single-junction amorphous silicon solar cell (Carlson and Wronski [5]) and from a recent "triple-junction" cell (Yang, Banerjee, and Guha [8]). The stabilized efficiency of the triple-junction cell is 13.0 %; the active area is 0.25 $cm^2$.

relatively modest electric fields that are "built in" to the device, and selenium and many other non-crystalline semiconductors proved unsuitable for making efficient cells. In Dundee, Scotland, Walter Spear and Peter LeComber discovered around 1973 that amorphous silicon prepared using a "glow discharge" in silane ($SiH_4$) gas had unusually good electronic properties; they were building on earlier work by Chittick, Sterling, and Alexander [3]. Glow discharges are the basis for the familiar "neon" light; under certain conditions, an electric voltage applied across a gas can induce a significant electrical current through the gas, and the molecules of the gas often emit light when excited by the current. Amorphous silicon was deposited as a thin film on substrates inserted into the silane gas discharge.* Spear and LeComber reported in 1975 [4] that amorphous silicon's conductivity could be increased enormously either by mixing some phosphine ($PH_3$) gas or some diborane ($B_2H_6$) gas with the silane. As for crystal silicon, the consequent phosphorus-doping of the amorphous silicon had induced a conductivity associated with mobile electrons (the material was "n-type"), and the boron-doping had induced a conductivity associated with mobile holes (the material was "p-type").

In 1974, at the Radio Corporation of America (RCA) Research Laboratory in Princeton, David Carlson discovered that he could make fairly efficient solar cells using a silane glow discharge to deposit films. In 1976 he and Christopher Wronski reported a solar cell based on

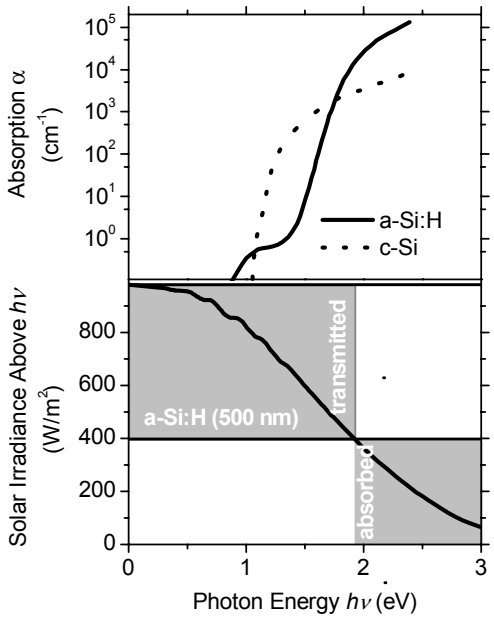


FIG. 2: (upper panel) Spectra of the optical absorption coefficient $\alpha(h\nu)$ as a function of photon energy $h\nu$ for crystalline silicon (c-Si) and for hydrogenated amorphous silicon (a-Si:H). After ref. [10]. (lower panel) Solar irradiance due to photons with energies greater than $h\nu$. The gray areas indicate the irradiance that is transmitted through, or absorbed by, a 500 nm a-Si:H film.

* The term "amorphous" is commonly applied to non-crystalline materials prepared by deposition from gases.

amorphous silicon [5] with a solar conversion efficiency of about 2.4 % (for historical discussion see ref. [6,7]).

Carlson and Wronski's report of the current density vs. output voltage is presented in FIG. 1 (along with the curve from a far more efficient cell reported in 1997 [8]). As these scientists had discovered, the optoelectronic properties of amorphous silicon made by glow discharge (or "plasma deposition") are very much superior to the amorphous silicon thin films prepared, for example, by simply evaporating silicon. After several years of uncertainty, it emerged that plasma-deposited amorphous silicon contained a significant percentage of hydrogen atoms bonded into the amorphous silicon structure, and that these hydrogen atoms were essential to the improvement of the electronic properties of the plasma-deposited material [9]. As a consequence, the improved form of amorphous silicon has generally been known as "hydrogenated amorphous silicon" (or, more briefly, a-Si:H). In recent years, many authors have used the term "amorphous silicon" to refer to the hydrogenated form, which acknowledges that the unhydrogenated forms of amorphous silicon are only infrequently studied today.

Why was there so much excitement about the amorphous silicon solar cells fabricated by Carlson and Wronski? First, the technology involved is relatively simple and inexpensive compared to the technologies for growing crystals. Additionally, the optical properties of amorphous silicon are very promising for collecting solar energy, as we now explain. In FIG. 2, the upper panel shows the spectrum for the optical absorption coefficients $\alpha(h\nu)$ for amorphous silicon and for crystalline silicon [10].* In the lower panel of the figure, we show the spectrum of the "integrated solar irradiance;" this is the intensity (in W/m$^2$) of the solar energy carried by photons above an energy threshold $h\nu$ [11].

We use these spectra to find out how much solar energy is absorbed by layers of varying thickness. The example used in the figure is an a-Si:H layer with a thickness $d$ = 500 nm. Such a layer absorbs essentially all photons with energies greater than 1.9 eV (the energy at which $\alpha = 1/d$). We then look up how much solar irradiance lies above 1.9 eV. Assuming that reflection of sunlight has been minimized, we find that about 420 W/m$^2$ is absorbed by the layer (the gray area labeled "absorbed"). 580 W/m$^2$ of energy is transmitted through such a layer. These energies may be compared to the results for c-Si, for which a 500 nm thick layer absorbs less than 200 W/m$^2$.

To absorb the same energy as the 500 nm a-Si:H layer, a c-Si layer needs to be much thicker. The implication is that much less material is required to make a solar cell from a-Si than from c-Si.† In the remainder of this section we first describe how amorphous silicon solar cells are realized in practice, and we then briefly summarize some important aspects of their electrical characteristics.

---

* We assume familiarity with the concept of a photon energy $h\nu$ and of an optical absorption coefficient $\alpha$; see chapter ??.

† The very different optical properties of c-Si and a-Si reflect the completely different nature of their electronic states. In solid state physics textbooks, one learns about the "selection rules" that greatly reduce optical absorption in c-Si, which is an "indirect bandgap" semiconductor. Such selections rules do not apply in a-Si. Additionally, the "bandgap" of a-Si is considerably larger than for c-Si.

## *1.2 Designs for Amorphous Silicon Solar Cells: A Guided Tour*

FIG. 1 illustrates the tremendous progress over the last 25 years in improving the efficiency of amorphous silicon based solar cells. In this section we briefly introduce three basic ideas involved in contemporary, high-efficiency devices: *(i)* the *pin* photodiode structure, *(ii)* the distinction between "substrate" and "superstrate" optical designs, and *(iii)* multijunction photodiode structures. A good deal of this chapter is devoted to more detailed reviews of the implementation and importance of these concepts.

### pin Photodiodes

The fundamental photodiode inside an amorphous silicon based solar cell has three layers deposited in either the *p-i-n* or the *n-i-p* sequence. The three layers are a very thin (typically 20 nm) p-type layer, a much thicker (typically a few hundred nm), undoped *intrinsic* (i) layer, and a very thin n-type layer. As illustrated in FIG. 3, in this structure excess electrons are actually donated from the n-type layer to the p-type layer, leaving the layers positively and negatively charged (respectively), and creating a sizable "built-in" electric field (typically more than $10^4$ V/cm).

Sunlight enters the photodiode as a stream of photons that pass through the p-type layer, which is a nearly transparent "window" layer. The solar photons are mostly absorbed in the much thicker intrinsic layer; each photon that is absorbed will generate one electron and one hole photocarrier [12,13]. The photocarriers are swept away by the built-in electric field to the n-type and p-type layers, respectively – thus generating solar electricity!

The use of a *pin* structure for a-Si:H based solar cells is something of a departure from solar cell designs for other materials, which are often based on simpler *pn* structures. For doped a-Si:H it turns out that minority photocarriers (holes in *n*-type a-Si:H, electrons in *p*-type a-Si:H) don't move very far, and so a *pn* structure would only collect photocarriers from photons generated in an extremely thin layer of doped a-Si:H. Indeed, in analyzing the performance of a-Si:H based solar cells, one normally considers any photons absorbed by the doped layers to be "wasted." The trick of keeping the doping atoms out of the absorber layer enables this layer to be thick enough to capture most of the sunlight.

In section 4 you will find a more detailed description of the device-physics of the *pin* solar cell; the description explains why the window layer is the p-type one, and also explains the design tradeoffs which determine the thickness of the absorber layer.

## Substrate and Superstrate Designs

One of the advantages of amorphous silicon based solar cells is that they absorb sunlight very efficiently: the total thickness of the absorbing layers in amorphous silicon solar cells is less than 1 micron. Consequently these layers need to be supported on a much thicker substrate. Two totally different designs for amorphous silicon solar cells have evolved corresponding to transparent and opaque substrates. We have illustrated the two designs in FIG. 3.

In the "superstrate" design, sunlight enters through the transparent substrate, which is usually glass or a transparent plastic. The insulating substrate needs a conducting layer, which is typically a "transparent conductive oxide" (TCO) such as $SnO_2$. The amorphous silicon photodiode layers are then deposited onto the TCO, starting with a p-type window layer. Finally, a "back" reflector is deposited onto the photodiode; the back reflector acts as an electrode to the top-most, n-type photodiode layer.

In the "substrate" design, sunlight enters the photodiode before it reaches the substrate. Starting with the substrate, the cell is fabricated in the reverse order compared to the superstrate design: first a back-reflector, then the photodiode layers (starting with an n-type layer), and finally a TCO layer to act as an electrode to the topmost, window layer of the photodiode.

These two designs permit a very wide range of application for amorphous silicon solar cells. The superstrate design (light enters through the substrate) is particularly suited to building-integrated solar cells in which a glass substrate can be used as an architectural element. The substrate design has generally been applied to solar cells using flexible, stainless steel substrates. The detailed construction of a deposition facility of course depends upon whether the substrate is rigid or flexible. Finally, it turns out that there is a profound effect of the substrate upon the properties of the first photodiode layers deposited upon it; this effect

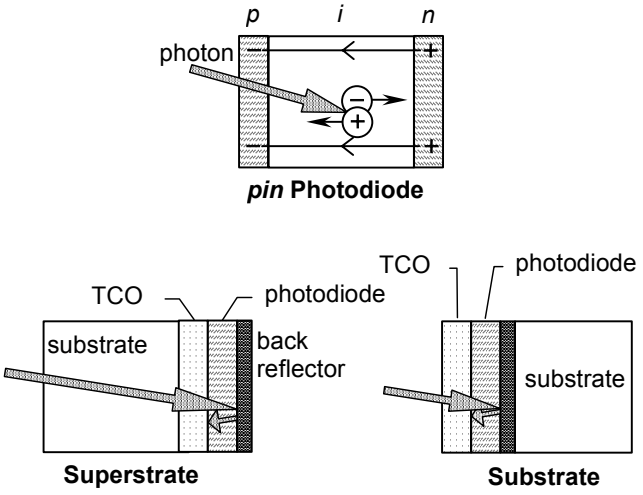


FIG. 3: In a *pin* photodiode, excess electrons are donated from the *n*-type to the *p*-type layers, leaving the charges and electric fields illustrated. Each photon absorbed in the undoped, intrinsic layer generates an electron and a hole photocarrier;. The electric field causes these carriers to drift in the directions shown. *pin* diodes are incorporated into solar cells in either the superstrate or substrate designs. For amorphous silicon based cells, photons invariably enter through the *p*-type window layer as shown here.

has led to fairly different photodiode structures for the superstrate and substrate designs.

### Multijunction Solar Cells

The conversion efficiency of the relatively simple, amorphous silicon *pin* photodiode structure just described can be significantly improved by depositing two or three such photodiodes, one on top of another, to create a "multijunction" device. We illustrate a "tandem" device in FIG. 4, which shows a combination of two *pin* diodes. [*] Note that the "bottom" cell is not based on a-Si:H, but rather upon an amorphous silicon-germanium alloy made by including germane ($GeH_4$) gas in the plasma-deposition recipe.

The main advantage to the tandem design over the simpler single-junction one is due to "spectrum splitting" of the solar illumination. Since the absorption coefficient for light rises rapidly with the photon energy, the topmost layer of a tandem cells acts as a "low-pass" optical filter. This effect is illustrated in FIG. 2, which shows that a 0.5 μm layer of a-Si:H absorbs photons with energies larger than 1.9 eV, and passes photons with smaller energies. The "wasted" lower energy photons can be efficiently harvested by amorphous silicon-germanium, which has a much larger absorption coefficient below 1.9 eV than does a-Si:H. Overall, the advantages of the multijunction design are sufficiently compelling that they usually overcome the additional complexity and cost of the deposition facility. Both tandem and triple-junction devices are being manufactured today. We discuss multijunction solar cells in detail in section 5.

## *1.3 Staebler-Wronski Effect*

One of the most intriguing and actively researched facets of amorphous silicon solar cells is the significant decline in their efficiency during their first few hundred hours of illumination. FIG. 5 illustrates this effect for a single-junction cell and for a triple-junction module made at United Solar Systems Corp. [14,15]. The single-junction cell loses about 30% of its initial efficiency after about 1000 hours; the triple-junction module loses about 15% of its initial efficiency.

All amorphous silicon based solar cells exhibit this type of initial behavior under

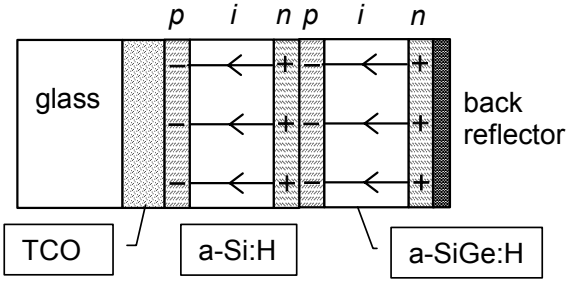


FIG. 4: A multijunction solar cell consisting of two *pin* solar cells deposited in series. Double-junction (or "tandem," as shown) and triple-junction designs can be significantly more efficient than single-junction designs. Substate texturing, which is important in real devices, is not indicated; see section 4.5.

[*] It is worth noting that the adjoining p-type and n-type layers do *not* form a p-n junction diode, but rather a simple Ohmic contact. We discuss the interesting physics underlying this fact in section 5.3.

illumination; the behavior is mostly due to the "Staebler-Wronski" effect [16], which is the light-induced change in hydrogenated amorphous silicon (a-Si:H) and related materials used in the cell. Although we have not illustrated it here, the Staebler-Wronski effect can be annealed away within a few minutes at temperatures of about 160 C (and the initial performance of the solar cell largely restored).

The Staebler-Wronski effect contributes to noticeable seasonal variations in the conversion efficiency of a-Si:H based modules in the field. In FIG. 6 we illustrate the daily average conversion efficiency and ambient temperature for a triple-junction module installation in Switzerland. The module performed best in hot weather. Up to 20 C, the relative increase in efficiency with temperature is about $+5 \times 10^{-3}$/K. It is noteworthy that there was no permanent degradation of this module over the three-year extent of the test. The conclusion that amorphous silicon modules reach a steady-state after about 1000 hours of steady illumination was also reached in a much larger study of modules manufactured by Advanced Photovoltaics Systems, Inc. [17].

This positive trend of efficiency with temperature is atypical of solar cells made with other materials; for example, the temperature-coefficient for crystal silicon solar cells is about $-4 \times 10^{-3}$/K [18,19]. Interestingly, if the temperature-dependence of a-Si:H solar cells is measured quickly – so that there is no time for the Staebler-Wronski effect to set in, the temperature-coefficient is also negative (about $-1 \times 10^{-3}$/K) [18]. The behavior of a module in the field may be understood as a competition of slow annealing of the Staebler-Wronski effect (which yields the positive temperature coefficient) and of a smaller, intrinsic negative coefficient [20,21].

## *1.4 Synopsis of this Chapter*

The remainder of this chapter is organized as follows. In section 2 we introduce some of the fundamental physical concepts required to interpret the scientific literature about amorphous silicon and related materials (such as amorphous silicon based alloys and, to a much lesser degree, microcrystalline silicon). Section 3 surveys the principal methods such as

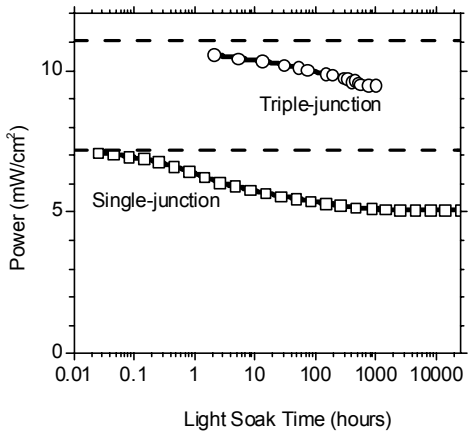


FIG. 5: The conversion efficiency in a-Si:H based solar cells declines noticeably upon the first exposure to sunlight. The figure illustrates this decline under a solar simulator (100 mW/cm$^2$) for a single-junction cell (260 nm i-layer thickness) and for a triple junction module made at United Solar Systems Corp. [14,15]; the dashed lines indicate the initial power measured for each device.

plasma deposition that are used to make amorphous silicon based solar cells. Section 4 describes how the simplest, single-junction solar cell "works," by which we mean how the photoelectric behavior of the cell is related to the fundamental concepts. High-efficiency solar cells based on amorphous silicon technology are multijunction devices, and in section 5 we discuss how these are made and how their performance can be understood and optimized. Section 6 describes some of the issues involved in manufacturing modules. To conclude this chapter, section 7 presents some of the directions which we consider to be important for future progress in the field.

There have been several excellent monographs and review chapters on amorphous silicon and amorphous silicon based solar cells in recent years. In the body of the chapter, we direct the reader to these works where we feel that they may be useful for expanded or complementary discussion.

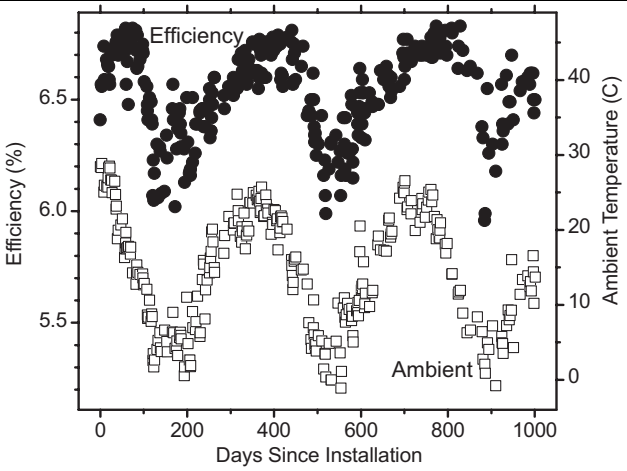


FIG. 6: Seasonal variations in the average conversion efficiency (solid symbols) of an amorphous silicon triple-junction module [22], along with the daily mean temperature (open symbols).

## 2 Atomic and Electronic Structure of Hydrogenated Amorphous Silicon

### *2.1 Atomic Structure*

Silicon atoms in amorphous silicon largely retain the same basic structure as for crystal silicon: each silicon atom is connected by covalent bonds to four other silicon atoms arranged as a tetrahedron. This understanding emerges from measurements of the scattering ("diffraction") of X-rays by the two materials [23] as well as from theoretical and computational studies of the two materials.

If you build a non-crystalline silicon structure with wooden sticks (to represent covalent bonds) and wooden balls drilled with four small holes for the sticks (to represent the silicon atoms), you will have some trouble in making a non-crystalline structure. To avoid a crystalline structure, you will need to bend the sticks. Quite soon, you will have to give up on the fourth stick on some atom, and you will have created an imperfect non-crystalline structure with a "dangling bond." Your problem is related to tetrahedral bonding: there are too many constraints on the positions of atoms to keep *all* bond lengths and angles reasonably close to the values demanded by silicon's chemistry in any non-crystalline structure. The same conclusion is reached by mathematical and computational methods [24,25]. Alloys such as $As_2Se_3$, which easily form non-crystalline glasses by cooling from a liquid, have an

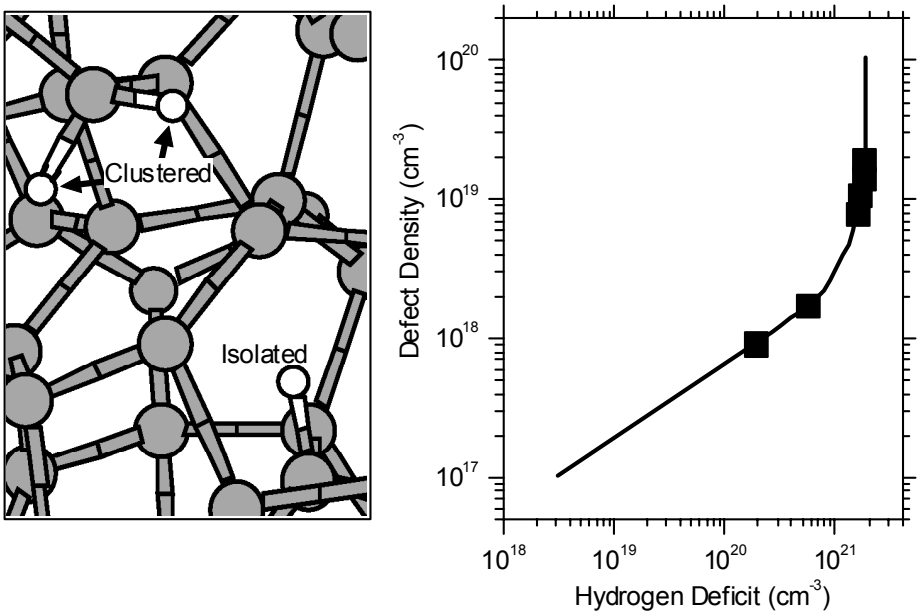


FIG. 7: (*left*) Computer model of the chemical bonding for hydrogenated amorphous silicon. The larger, gray spheres indicate Si atoms; the smaller, white spheres indicate hydrogen atoms, which are found in clustered and isolated configurations as indicated. (*right*) Correlation of the defect (dangling bond) density in a-Si:H with the density of hydrogen removed from the material by heating (the hydrogen deficit). The data points are derived from deuterium and defect profiles by Jackson, *et al* [33] (350 C deuteration). The curve is a fit to a model proposed by Zafar and Schiff [32].

average number of bonds per atom of about 2.7 or less.

For hydrogenated amorphous silicon (a-Si:H), silicon-hydrogen bonds resolve this structural problem. Several percent of the silicon atoms make covalent bonds with only 3 silicon neighbors; the fourth valence electron of the silicon bonds to a hydrogen atom. This crucial hydrogen is essentially invisible to X-rays, but is quite evident in non-destructive measurements (proton magnetic resonance [26] and infrared spectroscopy [27]) as well as destructive testing (secondary ion mass spectroscopy [28] and hydrogen evolution during annealing [29]).

There are quite a few distinct atomic configurations for the hydrogen in a-Si:H. The two principal "phases" of hydrogen evidenced by proton magnetic resonance are termed the "dilute" and "clustered" phases [26]. In the dilute phase a particular hydrogen atom is about 1 nm away from any other hydrogen atom; in the clustered phase there are two or more hydrogen atoms in close proximity. A computer calculation of a particular instance of this structure [30] is presented in FIG. 7. The densities of hydrogen in each of the individual phases, as well as the total density of hydrogen, depend upon the conditions under which the material is made.

## *2.2 Defects and Metastability*

While the underlying structure illustrated in FIG. 7 is non-crystalline, it is a chemically ideal structure: each atom forms the normal number of chemical bonds (four for silicon, one for hydrogen). This non-crystalline atomic structure largely determines the overall electronic and optical properties of the material, as we discuss shortly. However, many electronic properties in a-Si:H are also strongly affected by gross defects of chemical bonding. The atomic structure of the bonding defects in a-Si:H has been extensively studied using electron spin resonance. A single type of defect, the D-center, dominates most measurements in undoped a-Si:H [23]. The D-center is generally identified as a silicon dangling bond [31].

A dangling bond may be envisioned using FIG. 7: just imagine that the hydrogen atom is removed from the dilute-phase site in the lower right-hand corner of the figure, leaving behind a single unbonded electron (the "dangling bond"). This simple picture is consistent with the following observation: the density of dangling bonds increases when hydrogen is removed from a-Si:H by heating. We present a comparison of a model for this relationship together with measurements illustrating the effect in FIG. 7 [32,33]. Note that the density of dangling bonds is generally much lower than the density of hydrogen lost from the structure; this effect has been attributed to the evolution of hydrogen from clustered-phase sites, which presumably does not create dangling bonds.

The most intense defect research in a-Si:H has not been focused on the direct hydrogen-

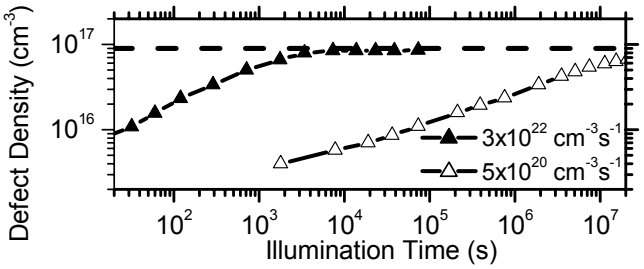


FIG. 8: Plot of the defect (dangling bond) density during extended illumination of an a-Si:H film as measured by Park, Liu, and Wagner [34]. Data are given for high and low-intensity illumination; the legend indicates the photocarrier generation rate for each intensity.

defect relation, but rather on the light-soaking effects. We illustrated how light-soaking degrades the solar conversion efficiency in FIG. 5, and in FIG. 8 below we illustrate how it increases the defect density. For the high intensity illumination, the defect density reaches a steady-state at about $10^{17}$ $cm^{-3}$. For engineering purposes, it is very important that a-Si:H reaches such a "stabilized" condition after extended light-soaking.

Although the defect density is not the only property of a-Si:H modified following light-soaking [35], most workers believe that the principal cause of the Staebler-Wronski effect is this increase in dangling bond density after light-soaking. The close connection between hydrogen and defects in a-Si:H has led to several efforts to understand the defect creation in terms of metastable configurations of hydrogen atoms [35,36]. The idea is that illumination provides the energy required to shift hydrogen atoms away from their dilute-phase sites, thus creating dangling bonds. The technological importance of establishing the atomic mechanism underlying the Staebler-Wronski effect lies in the possibility that this effect can be mitigated in a-Si:H by changing its preparation conditions.

An essential feature of the light-soaking effects on a-Si:H cells and films is that most of the effects are "metastable," and can be removed nearly completely by annealing of a light-soaked sample at a temperature above 150 C. More generally, the stabilized condition of a-Si:H cells and films is quite temperature-dependent. For example, FIG. 6 showed that the module efficiency is substantially affected by the seasons, and is highest following the hottest days. The measurement may be understood by considering that the stabilized condition is due to competition between two rates: the creation of metastable defects by light, and a thermally activated process which anneals them away.

## 2.3 Electronic Density-of-States

The most important concept used in understanding the optical and electronic properties of semiconductors is the electronic density-of-states, *g(E).* The idea is a simple approximation: if a single electron is added to a solid, it may be viewed as occupying a well-defined state (or molecular "orbital") at a particular level energy $E$. In a range of energies $\Delta E$, the number of such states per unit volume of the solid is $g(E)\Delta E$.

In FIG. 9 we have illustrated the density-of-states for hydrogenated amorphous silicon as it has emerged primarily from measurements of electron photoemission [37,38], optical absorption [39], and electron and hole drift mobilities [40]. In the dark at low temperatures, the states with energies below the Fermi energy $E_F$ are filled by electrons; above the Fermi energy the states are empty. There are two strong bands of states illustrated: an occupied valence band ($E<E_V$), originating with the Si-Si and Si-H bonding orbitals, and an unoccupied conduction band ($E>E_C$ ), originating with "antibonding" orbitals.

## 2.4 Bandtails, Bandedges, and Bandgaps

Between the conduction and valence bands lies an "energy gap" where the density-of-states is very low. Any functional semiconductor, crystalline or non-crystalline, must have such an energy gap. For perfect crystals, the valence and conduction bandedge energies $E_V$ and $E_C$ are well defined, as is the *bandgap* $E_G = E_C - E_V$. Interestingly, in disordered semiconductors there are exponential distributions of bandtail states near these bandedges. For the valence bandtail we write $g(E) = g_V \exp\left(-\left(E - E_V\right)/\Delta E_V\right)$. The width $\Delta E_V$ of this exponential distribution is important in interpreting optical absorption experiments, where it is usually identified with the exponential "Urbach" tail of the spectrum apparent in FIG. 2. For a-Si:H, a typical value $\Delta E_V = 50 \times 10^{-3}$ eV. $\Delta E_V$ is also used to account for the very slow drift

of holes in an electric field ie. the hole *drift-mobility*); [40,41]. The conduction bandtail width $\Delta E_C$ is much narrower; for the best a-Si:H materials it is about $22\times10^{-3}$ eV, but increases markedly for amorphous silicon-germanium [42].

Given the presence of exponential bandtails, the very existence of a bandedge energy can reasonably be questioned. Remarkably, detailed analysis of drift-mobility measurements supports the concept of a well-defined bandedge [40,43]. Most workers consider the bandedge to be the energy that separates electron orbitals that are localized (ie. have well defined locations in space) from orbitals that are delocalized. The bandedges are correspondingly termed the conduction and valence band *mobility edges* [44].

Unfortunately, for non-crystalline semiconductors there is no single, conclusively established procedure for locating the bandedges within the density-of-states. The bandgap is thus difficult to determine without some ambiguity. Since amorphous silicon based materials with varying bandgaps are used in solar cells, it is nonetheless very important to establish conventional procedures for comparing bandgaps. By far the most common approach is to analyze measurements of the optical absorption coefficient $\alpha(h\nu)$ similar to those in FIG. 2; one typical analysis yields an "optical" or "Tauc" bandgap $E_T$ [45]

$$\alpha(h\nu) = (A/h\nu)(h\nu - E_T)^2 \ . \qquad (1)$$

The proportionality constant $A$ incorporates several effects, and is not usually studied separately.

The bandgap obtained using this procedure is typically about 1.75 eV in a-Si:H, but varies substantially with deposition conditions and alloying with germanium or carbon. A simpler procedure than that of Tauc is to define the bandgap to be the photon energy corresponding to a particular optical absorption coefficient $\alpha$; using $\alpha = 3\times10^3$ cm$^{-1}$ yields values (denoted as $E_{3.5}$) similar to the Tauc procedure. Finally, there is undoubtedly a difference between these optical estimates of the bandgap and the true, "electrical" bandgap

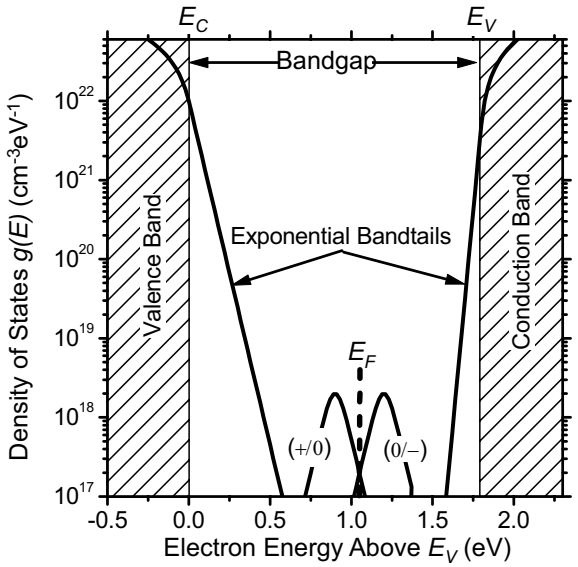


FIG. 9: Density of electronic states *g(E)* in hydrogenated amorphous silicon. The shaded areas indicate delocalized states in the bands; these bands themselves have tails of localized states with an exponential distribution. Midway between the bands are levels belonging to gross defects such as dangling Si bonds.

$E_G = E_C - E_V$. Internal photoemission measurements [46] indicate that the electrical bandgap is 50-100 meV larger than the Tauc bandgap.

## 2.5 Defects & Gap States

Between the bandtails lie defect levels; in undoped a-Si:H, these levels appear to be due entirely to the dangling bonds ("D-centers") measured by electron spin resonance. For example, infrared absorption at photon energies around 1.2 eV is sensitive to the optical processes which detach an electron from a defect and promote it to the conduction band, or which transfer an electron from the valence band to a defect. This infrared signal is visible in FIG. 2; for samples of varying electronic properties, the infrared absorption coefficient is proportional to the *D*-center density over a range of at least 100 [47].

The next issue to be resolved is the positions of the corresponding levels, as illustrated in FIG. 9. The *D*-center is "amphoteric:" there are three charge states (with +e, 0, and –e charges), leading to two levels (transitions between the 0/+ and –/0 charge states). A *rough* guide to level positions estimated under near-dark conditions is the following. The (–/0) level is about 0.6 eV below $E_C$ in low defect-density, undoped a-Si:H [49]. The (+/0) level lies about 0.3 eV below the (–/0) levels; the difference between the 2 levels is usually termed the "correlation energy" of the *D*-center [48]..

The actual level positions apparently vary between doped and intrinsic a-Si:H [23], between intrinsic samples with varying densities of *D*-centers [49], and possibly between dark and illuminated states [50].

## 2.6 Doping

Doped layers are integral to *pin* solar cells. Doping itself, which is the intentional incorporation of atoms like phosphorus and boron in order to shift the Fermi energy of a material, works very differently in amorphous silicon than in crystals. For example, in crystalline silicon (c-Si), phosphorus (P) atoms substitute for silicon atoms in the crystal lattice. P has five valence electrons, so in the "fourfold coordinated" sites of the Si lattice, four electrons participate in bonding to neighboring silicon atoms. The fifth "free" electron occupies a state just below the bottom of the conduction band, and the dopants raise the Fermi energy to roughly this level.

In a-Si, most phosphorus atoms bond to only three silicon neighbors; they are in "threefold coordinated" sites. This configuration is actually advantageous chemically; phosphorus atoms normally form only 3 bonds (involving the 3 valence electrons in "p" atomic orbitals). The final two electrons are paired in "s" atomic orbitals, do not participate in bonding, and remain tightly attached to the P atom. The reason that this more favorable bonding occurs in a-Si, but not in c-Si, is the absence of a rigid lattice. As a thin-film of a-Si grows, the network of bonds adjusts to incorporate impurity atoms in nearly ideal chemical arrangement. In c-Si, it would be necessary to grossly rearrange several Si atoms in the lattice, and to leave a number of dangling Si bonds, in order to accommodate the P atom in this configuration. The extra energy for this rearrangement is larger than would be gained from more ideal bonding of P, and substitutional doping is favored.

Thus phosphorus doping is a paradox in amorphous silicon. It is, at first, unclear why it occurs at all, since doping involves fourfold coordinated P, and P atoms are generally threefold coordinated in a-Si. This puzzle was first solved in 1982 by Street, who realized that independent formation of both a positively charged, fourfold coordinated $P_4^+$ and a

negatively charged dangling bond $D^-$ can occur occasionally instead of the more ideal threefold coordination [23]. This understanding leads to two important consequences. First, doping is inefficient in a-Si; most dopant atoms do not contribute a "free" electron, and do not raise the Fermi energy. Second, for each dopant atom which does contribute an electron, there is a balancing, Si dangling bond to receive it. These defect levels lie well below the conduction band, so the fourfold-coordinated phosphorus atoms are less effective in raising the Fermi energy than in c-Si. Additionally, the negatively charged dangling bonds induced by doping are very effective traps for holes. Since bipolar transport of both electrons and holes is essential to photovoltaic energy conversion, photons absorbed in doped layers don't contribute to the power generated by solar cells.

## *2.7 Alloying & Optical Properties*

The structural and optical properties we have described can be varied substantially by changes in deposition conditions. For example, changing the substrate temperature or the dilution of silane by hydrogen (in plasma deposition) causes a change in the the optical bandgap for a-Si:H films over at least the range 1.6 – 1.8 eV [51]; these changes can be ascribed to changes in the hydrogen microstructure of the films. Even larger changes can be effected by alloying with additional elements such as Ge, C, O, and N; alloying is readily accomplished by mixing the silane ($SiH_4$) source gas with gases such as $GeH_4$, $CH_4$, $O_2$ or $NO_2$, and $NH_3$, respectively. The resulting alloys have very wide ranges of bandgaps, as we illustrate for a-$Si_{1-x}Ge_x$:H below. For simplicity, we shall usually refer to these alloys using the abbreviated notation: a-SiGe for a-$Si_{1-x}Ge_x$:H, etc..

Only some of these materials have proven useful in devices. In particular, a-SiGe alloys with optical gaps down to about 1.45 eV are employed as absorber layer in multijunction *pin* cells; the narrower bandgap of a-SiGe compared to a-Si allows for increased absorption of photons with lower energies [52]. FIG. 10 (left panel) illustrates how the spectrum of the absorption coefficient $\alpha(h\nu)$ changes for a-SiGe alloys with different atomic percentages $x$; the different optical bandgaps are indicated as labels. Two features of these data should be noted. First, the Urbach slopes remain constant (at about 50 meV) over the entire range of

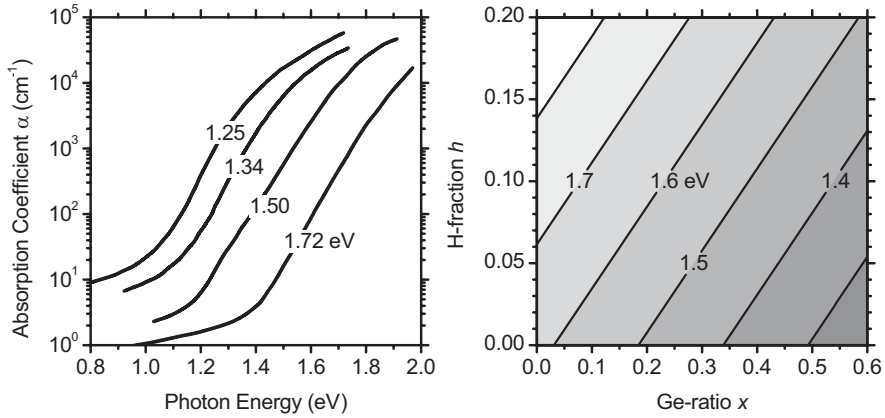


FIG. 10: (*left*) Absorption coefficient spectra for a-SiGe alloys; the optical bandgaps and corresponding Ge fractions $x$ are: 1.25-0.58, 1.34-0.48, 1.50-0.30, 1.72-0.0 [52]. (*right*) Typical optical bandgaps for a-$Si_{1-x}Ge_x$:H alloys for varying Ge-ratio $x$ and atomic fraction $h$ of hydrogen.

bandgaps. Second, the plateau in the absorption coefficient at the lowest photon energies are indicative of the defect density, which indicates that this density increases steadily as the bandgap diminishes.

FIG. 10 (right panel) is a contour plot showing how the optical bandgap of a-$Si_{1-x}Ge_x$:H varies with the Ge-ratio *x* and with atomic fraction *h* of hydrogen. The figure reflects experimental results for a-Si:H alloys of varying H-fraction [51] and for a-SiGe:H alloys for which both *x* and *h* were reported [53].* Note that, for constant fraction *h,* the bandgap decreases about 0.7 eV as the Ge-ratio *x* increases from 0 to 1. The bandgap increases with atomic fraction of hydrogen *h*. FIG. 10 should be viewed as a useful approximation; in particular, the atomic fraction *h* is only one aspect of the hydrogen microstructures in a-SiGe alloys, and quantitative deviations from the contour plot are likely. Additionally, only some of the materials represented in the figure are useful as absorber layers. In particular, as the Ge ratio *x* rises to about 0.5, the optoelectronic properties become so poor that these alloys are no longer useful in solar cells[54]. Similarly, only limited ranges of the atomic fraction of hydrogen *h* yield useful absorber layers.

It might be thought that a-SiC would be equally useful as a wider bandgap absorber; despite some promising research [55], this material is not being used as an absorber layer by manufacturers. B-doped a-SiC is used extensively as a p-type, window layer [56]. a-SiO and a-SiN are used as insulators in thin film transistors [57], but are not major components in solar cells.

* FIG. 10 is based on the function $E_G = 1.62 + 1.3h - 0.7x$ obtained by fitting to experimental results reported by Hama, *et al.* [51] and Middya, *et al.* [53].

## Section 3 Depositing Amorphous Silicon

### *3.1 Survey of Deposition Techniques*

The first preparations of a-Si:H by Chittick, *et al*. [58] and by Spear and LeComber [59] used a silane-based glow discharge induced by radio-frequency (RF) voltages; the method is now often termed plasma enhanced chemical vapor deposition (PECVD). Since this pioneering work, many deposition methods have been explored with the intention of improving materials quality and deposition rate. Among these methods, PECVD using 13.56 MHz excitation is still the most widely used today in research and manufacturing of a-Si based materials. However, emerging film deposition methods, mostly toward higher deposition rate or toward making improved microcrystalline silicon films, have been extensively explored in recent years. Table 1 summarizes the most extensively studied deposition processes used as well as some of their advantages and disadvantages. Among these, PECVD with very high frequency (VHF) and hot-wire catalytic deposition process (HW) will be further discussed in this section due to their potential for use in future high-throughput solar cell manufacturing.

### *3.2 RF Glow Discharge Deposition*

FIG. 11 shows a schematic of a typical RF PECVD chamber and related parts. A silicon containing gas such as a mixture of $SiH_4$ and $H_2$ flows into a vacuum chamber that is evacuated by a pump. Two electrode plates are installed inside, and an RF power is applied between them; one option is to ground one of these electrodes. At a given RF voltage across

Table 1: Various deposition processes used for depositing amorphous silicon based materials

| **Processes** | **Max. Rate*** | **Advantages** | **Disadvantages** | **Manufac.** | **Refs** |
|---|---|---|---|---|---|
| RF PECVD | 3 Å/s | high quality uniform | slow | Many | 60, 61, 62 |
| DC PECVD | 3 Å/s | high quality uniform | slow | BP Solar | 63, 64 |
| VHF PECVD | 15 Å/s | fast | poor uniformity | None | 65, 66 |
| Microwave PECVD | 50 Å/s | very fast | film quality not as good | Canon | 67 |
| Hot-wire | 50 Å/s | very fast | poor uniformity | None | 68, 69 |
| Photo-CVD | 1 Å/s | high quality | slow | None | 70, 71 |
| Sputtering | 3 Å/s | | poor quality, slow | None | 72, 73 |

[+]Max. Dep. Rate: The deposition rate beyond which the film quality deteriorates rapidly; these numbers are empirical, not fundamental limits, and represent current results at the time of publication.

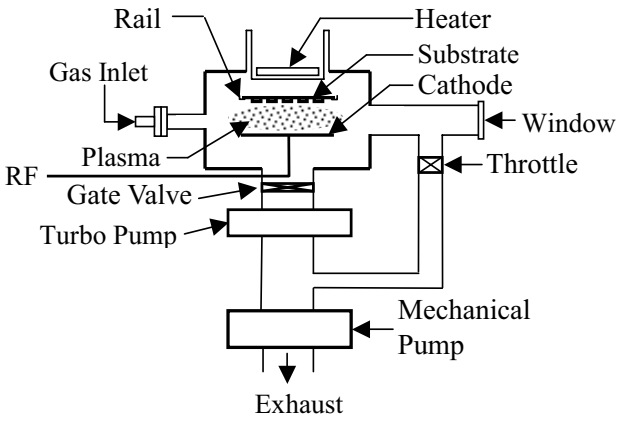

FIG. 11: Schematic of a typical RF glow discharge deposition chamber.

the plates, there is usually a range of gas pressures for which a plasma will occur. The plasma excites and decomposes the gas and generates radicals and ions in the chamber. Various substrates may be mounted on one or both of the electrodes, and thin hydrogenated silicon films grow on the substrates as these radicals diffuse to them. The substrates are heated to achieve optimum film quality; this effect is attributed to thermally activated surface diffusion for adatoms on the growing film.

A PECVD system usually consists of several major parts: (i) a gas delivery system (gas cylinders, pressure regulators, mass flow controllers, and various gas valves to direct gas flows); (ii) a deposition chamber that has electrodes, substrate mounts, substrate heaters, and the RF power feedthrough; (iii) a pumping system that usually has a turbomolecular pump backed with a mechanical pump; (iv) a pressure control system that has a capacitance manometer, ionization gauges, thermocouple gauges and/or throttle valve to monitor and control the chamber pressure; (v) an exhaust system for the process gases (typically either with a chemical scrubber to neutralize the gases, or a "burn box" to pyrolyze them). In multi-chamber systems there is a transfer system to move substrates inside the vacuum system between various deposition chambers through appropriate gate valves. Many of these elements are connected to an instrument control panel that contains an RF power supply, impedance matching box, and readouts or controllers for the vacuum gauges, mass flow controllers, throttle valves, pneumatic valves and turbomolecular pumps.

The film growth in a PECVD process consists of several steps: source gas diffusion, electron impact dissociation, gas-phase chemical reaction, radical diffusion and deposition [60,74,61]. To deposit good quality a-Si films, the deposition conditions need to be controlled within certain ranges desirable for high quality a-Si growth. Typical ranges of parameters for a-Si are summarized in Table 2.

Table 2: Ranges of rf-PECVD deposition conditions for a-Si:H films with optimal properties. These numbers are empirical, not fundamental limits, and represent current results at the time of publication

| Range | Pressure (Torr) | RF power density ($W/cm^2$) | Substrate Temp. (C) | Electrode spacing (cm) | Active gas flow* ($sccm/cm^2$) | $H_2$ dilution R** |
|---|---|---|---|---|---|---|
| Upper | 2 | 100 | 350 | 5 | 0.02 | 100 |
| Medium | 0.5 | 20 | 250 | 3 | 0.01 | 10 |
| Lower | 0.05 | 10 | 150 | 1 | 0.002 | 0 |

*Flows of active gases, such as $SiH_4$, $GeH_4$ or $Si_2H_6$, for each unit area of the deposition area (electrode + substrate + chamber walls).
**Hydrogen dilution R, defined here as the ratio of hydrogen and active gas flows (e.g. $H_2/SiH_4$)

The pressure range is usually between 0.05 Torr and 2 Torr. Lower pressure is desirable for making uniform deposition, and higher pressure is more desirable for preparing microcrystalline silicon films. Most researchers use a pressure between 0.5 – 1 Torr for a-Si deposition. The RF power should be set at around 10 $mW/cm^2$ to 100 $mW/cm^2$ for a capacitively coupled reactor. Below 10$mW/cm^2$, it is difficult to maintain a plasma. Higher power is desirable for higher deposition rate. However, above 100 $mW/cm^2$, the rapid reactions in the gas can create a silicon polyhydride powder that contaminates the growing Si film. This problem can be mitigated by using very low pressure or strong hydrogen dilution.

The substrate temperature is usually set between 150 to 350 $^oC$. At lower substrate temperature, more H is incorporated in the film. As expected from FIG. 10, this increases the bandgap of a-Si:H slightly higher [51,75]. However, lower substrate temperature (< 150 C) exacerbates silicon polyhydride powder formation unless high hydrogen dilution is used. At higher substrate temperature, less hydrogen is incorporated and the bandgap is somewhat reduced. These effects are attributed to the thermal enhancement of the surface diffusivity of adatoms during growth; presumably at higher temperatures the silicon network is more ideal, and binds less hydrogen. Researchers exploit the substrate temperature effect on the bandgap in device making. Wider bandgap materials are useful in the top component cell of a triple-junction solar cell [76, 77]. Narrower bandgap materials are useful as the top cell i-layer of an a-Si/a-SiGe tandem cell. However, at temperatures higher than 350 $^oC$ the quality of the material degrades; this effect is attributed to loss of hydrogen passivation of dangling bonds.

The electrode spacing in an RF glow discharge reactor is usually set between 1 cm and 5 cm for a-Si deposition. Smaller spacing is more desirable for a uniform deposition, while with a larger spacing it is easier to maintain a plasma. The flow rate that is required is determined by deposition rate and the area of the reactor plates. Some of the silicon atoms in the gases directed into the chamber are deposited onto the substrates or the chamber walls; the remainder gets pumped to the exhaust. Manufacturers may prefer conditions that lead to higher gas utilization (lower gas flows and higher RF power). But this compromises the quality of a-Si films deposited near the downstream area when a linear flow scheme is used. For an R&D type deposition system with a 200-$cm^2$ electrode area and for the deposition of a-Si at the rate of 0.1 nm/s, a few sccm (cubic centimeters per minute at atmospheric pressure) of $SiH_4$ flow is typical. As one may easily calculate, for such a chamber with an electrode diameter of 16 cm and an electrode gap of 2.54 cm, 1 sccm of $SiH_4$ (or 0.005 $sccm/cm^2$ for this chamber) for a 1 Å/s deposition rate corresponds to a gas utilization of 11%. For the

deposition of high quality, stable a-Si material, a hydrogen dilution at appropriate level is usually used, as will be discussed in Section 3.6.

Another important aspect for the growth of high quality a-Si films is the reduction of contaminants, such as oxygen, carbon, nitrogen, or metal elements. Fortunately, due to the flexibility of the bonding network in an amorphous solid, the tolerance level for contaminants in a-Si is much higher than its crystalline counterpart. For example, for one of the cells (with a 1.84 eV intrinsic layer) whose optoelectronic behavior is shown in FIG. 23, a SIMS measurement [78] reveals that the intrinsic layer has concentrations of O, C, N around $1.3x10^{19}$, $2.2x10^{18}$ and $1.7x10^{17}/cm^3$. Despite these contamination levels, this cell has a very good efficiency; the contamination levels indicated are typical for a-Si based i-layers. However, when the amount of contaminants are higher than these in the i-layers, the device performance, particularly the fill-factor, will suffer due to reduced diffusion length of photogenerated carriers.

To understand and monitor the film growth in a PECVD process, various spectroscopic tools, including optical emission spectroscopy [79], optical absorption spectroscopy [80] and residual gas analyzer [81] have often been used to measure the plasma and the concentration of various species inside the reactor. It is believed that the $SiH_3$ radical is mostly responsible for the growth of high quality a-Si film [82]. Such spectroscopic tools could be useful in studying and monitoring the active species and contaminants during growth.

RF glow discharge systems may be designed with different geometries based on specific needs and deposition requirements. While in R&D process the substrates and electrode are usually placed horizontally, in manufacturing processes the substrates are often installed vertically for high throughput production.

## *3.3 Glow Discharge Deposition at different frequencies*

The standard RF frequency for glow discharge deposition is $f$=13.56 MHz, which is a frequency allotted for industrial processes by federal and international authorities. A much larger frequency range has been explored, including DC ($f$ = 0), low frequency ($f$~kHz), very

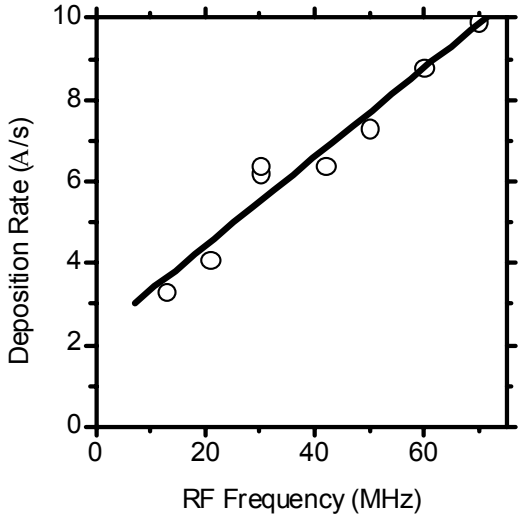


FIG. 12: Deposition rate for a-Si:H films as a function of RF excitation frequency (at constant power); after Shah, *et al.* [83]

high frequency (VHF) ($f$~ 20 –150 MHz), and microwave frequency (MW) ($f$ = 2.45 GHz). DC glow discharges were used in the early days of amorphous silicon at RCA Laboratories, and they are presently used in manufacturing at BP Solar, Inc. [63, 64]. AC glow discharge, including RF, VHF and MW PECVD, are more widely used due to the relative ease in maintaining the plasma and to more efficient ionization. VHF and MW deposition have been intensively studied because of the higher deposition rate both for amorphous and, recently, for microcrystalline and polycrystalline silicon films. In the following, we discuss the use of VHF and MW PECVD for a-Si deposition.

### VHF Glow Discharge Deposition

The group at Université de Neuchatel [65,83] has pioneered VHF plasma as a route to higher deposition rates. FIG. 12 shows a linear increase in the deposition rate of a-Si films as a function of plasma excitation frequency (under constant plasma power). One key to the success of this approach is that higher excitation frequency enables researchers to deposit a-Si films at rates exceeding 1 nm/s without making polyhydride powder, as is found when deposition rates are increased by increasing RF power at a lower frequency.

The exact reasons for the high-rate, powder-free deposition of a-Si using a VHF plasma are not well understood. At this moment, it is thought that the beneficial effect is due to an enhancement in the high-energy tails of the electron energy distribution function of the plasma [66,84].

High-quality films and devices have been obtained using VHF deposition [83, 66,85]. Table 3 compares four single-junction solar cells with intrinsic layers fabricated using low and high frequencies and low and high RF power; otherwise the deposition conditions were identical. While for low-power deposition the cell performances are similar, at high deposition rate, the VHF-produced devices are much superior. The ability to make high quality a-Si material at high rate using VHF could be very important for high throughput manufacturing.

Although the advantages of using VHF deposition for high-rate growth have been clearly demonstrated, VHF process has not yet been used in large-scale production as of the publication time of this book. There are two principal challenges to applying VHF deposition in manufacturing. 1) Non-uniform deposition on a large, production-scale substrate. RF standing waves may be formed on the electrode when the electrode size is comparable to half the wavelength of the RF wave. 2) VHF coupling. It is fairly difficult to couple VHF power from the generator to large electrodes. Several research groups are working in this area and have made significant progress [86].

Table 3: Comparison of solar cell properties for cells with i-layers deposited using RF and VHF frequencies and different deposition rates. The VHF-deposited devices are superior at high deposition rate. After [85].

| Excitation Frequency (MHz) | Dep. Rate (A/s) | Initial Cell Power ($mW/cm^{2)}$ | Degradation (%) |
|---|---|---|---|
| RF (13.56) | 0.6 | 6.6 | 14 |
| VHF (70) | 10 | 6.5 | 10 |
| RF (13.56) | 16 | 5.3 | 36 |
| VHF (70) | 25 | 6.0 | 22 |

### Microwave Glow Discharge Deposition

Glow discharge deposition at a microwave frequency of 2.45 GHz has also been studied [87, 88]; as expected from FIG. 12, very high deposition rates are obtained. When the MW plasma was in direct contact with the substrate, the deposited films had poor optoelectronic properties compared with RF-deposited films, and were not suitable as intrinsic layers for high-efficiency solar cells. *Remote* MW excitation has also been studied [89], and high quality films have been obtained. In remote plasma deposition processes, substrates are placed outside the plasma region. The MW plasma is used to excite or decompose a carrier gas such as He, Ar, or $H_2$ that passes through the MW zone toward the substrates. The excited carrier gas then excites $SiH_4$ or $Si_2H_6$ directed into the chamber near the substrates. Using such an indirect excitation process, the concentration of $SiH_3$ radicals can be maintained while the concentrations of other radicals ($SiH_2$, SiH, etc.) can be minimized. However, the high deposition rate of the direct plasma deposition is also reduced with remote plasmas. MW plasma deposition has been studied at United Solar [90] and Canon [91,92], and is used for the deposition of some of the i-layers in Canon's 10 MWp triple-junction production line. Generally, the structural and optoelectronic properties of MW-deposited a-Si based films are poorer than RF-deposited films. However, at a very high deposition rate, e.g. 50 Å/s, the MW-deposited films will be superior than films made using RF and VHF deposition.

## *3.4 Hot-wire Chemical Vapor Deposition*

Several years after Hot-Wire Chemical Vapor Deposition (HWCVD) was introduced [93, 68], Mahan, *et al.* [69] improved the deposition process and produced a-Si films with superior materials performance. Since then, HWCVD has been studied and used in experimental scale worldwide for depositing high quality a-Si and μc-Si based films at high rate. The setup for a HWCVD system is similar to the schematic shown in FIG. 11 for RF-PECVD except that the RF electrode is replaced with a heated filament. In a HW process, $SiH_4$ gas or a mixture of $SiH_4$ and other gases such as $H_2$ or He is directed into the chamber. The gas is catalytically excited or decomposed into radicals or ions by a metal filament heated to a high temperature (around 1800-2000 $^oC$). The silicon radicals then diffuse inside the chamber and deposit onto a substrate placed a few centimeters away and heated to an elevated temperature of 150 to 450 $^oC$. Mahan, *et al*. demonstrated that HWCVD deposited a-Si materials show relatively lower H content in the film and improved light stability compared with RF PECVD films [69]. The improved HWCVD deposited a-Si has been incorporated in an n-i-p solar cell as the intrinsic layer and solar cells with ~10% initial efficiency have been demonstrated [94,95].

HWCVD is considered very promising. Although it has not yet been incorporated into any of today's large scale manufacturing facilities, the ability to deposit a-Si and a-SiGe films at very high rate (~up to 150-300 Å/s) [96, 97] has attracted tremendous interest. Another reason researchers are interested in HW CVD is its effectiveness in making micro- and poly-crystalline silicon films.

There are several concerns about incorporating HW processes in manufacturing. First, the uniformity of HW films is still poorer than that of RF PECVD films, although some companies have worked on it and made significant improvement [98]. Second, the filament needs to be improved to reduce the maintenance time in production. Third, HW-deposited solar cells have not yet achieved the same performance as cells prepared using low deposition-rate, RF PECVD.

### 3.5 Other Deposition Methods

Beside PECVD and HW deposition methods, other deposition processes have been explored for depositing a-Si films. These include (i) reactive sputter deposition from silicon targets using a mixture of hydrogen and argon [99, 100]; (ii) e-beam evaporation, assisted with various hydrogenation methods [101, 102], (iii) spontaneous chemical vapor deposition [103], (iv) photo-CVD [70, 71] using ultraviolet excitation and mercury sensitization, (v) remote-plasma chemical vapor deposition [104], (vi) electron cyclotron resonance (ECR) microwave deposition [105, 106], (vii) pulsed laser deposition [107, 108], and (viii) gas jet deposition [109]. Most of these deposition methods yield poorer a-Si films or solar cells compared with RF PECVD deposited films and devices, therefore, are not (or not yet) used in large scale a-Si PV production.

### 3.6 Hydrogen Dilution

Strong hydrogen dilution of the silane gas mixture during a-Si deposition has been found to reduce the density of defect states and improve the stability of the material against light-soaking effects [110, 111, 112]. Solar cells with i-layers deposited using strong $H_2$ dilution show improved performance and stability [113, 114]. There are two other important effects of hydrogen dilution. As the dilution is increased, the deposition rate declines. When hydrogen dilution is increased sufficiently, the thin silicon films which are deposited become

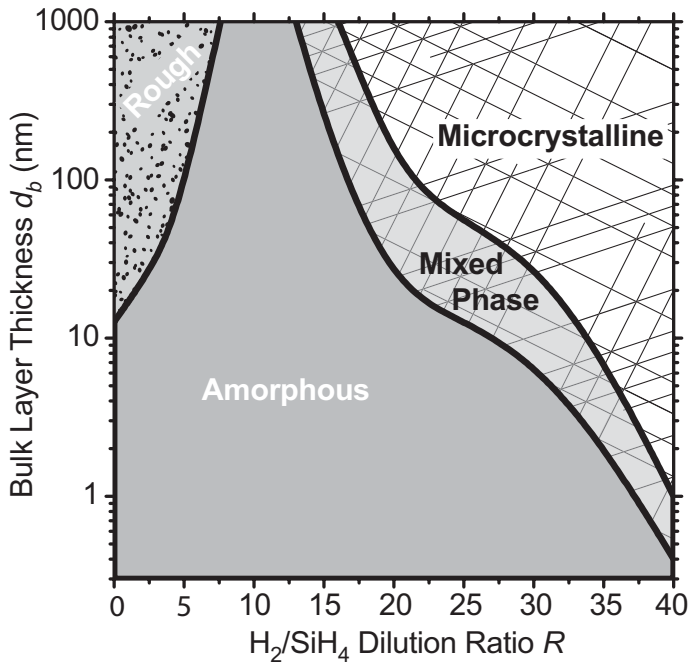


FIG. 13: Phase diagram for the structure of plasma-deposited silicon thin films for varying dilution ratios $R$ of silane in hydrogen and film thickness $d_b$; thin films were deposited onto a single-crystal Si substrate. For lower dilutions ($R < 10$) the films remain amorphous, but undergo a roughening transition in thicker films. For high dilutions films start out as amorphous, develop into a mixed phase of amorphous silicon and silicon crystallites, and ultimately become entirely microcrystalline. Based upon the phase diagram proposed by Ferlauto, *et al.* [115] on the basis of *in-situ* spectroscopic ellipsometry measurements.

microcrystalline.

Ferlauto, *et al*. [115] have made a careful study of the "phase diagram" for silicon thin films deposited under varying levels of hydrogen dilution of silane. Some of their results, which are based on *in situ* spectroscopic ellipsometry of the growing film, are presented as FIG. 13; this diagram pertains to a particular RF power level, substrate (c-Si), and substrate temperature. For lower dilutions ($R$<10) , films are invariably amorphous, but there is a transition to a "roughened" surface beyond a critical thickness. This roughening transition is suppressed as dilution is increased. For higher dilutions, the growing thin film first adopts an amorphous structure. As the film thickens, crystallites form in the amorphous matrix (creating a "mixed phase.") Ultimately, the film becomes entirely microcrystalline. The details of the phase diagram do depend upon the details of deposition, in particular upon power and substrate conditions, but the structure of the phase diagram is thought to be universal.

These effects of hydrogen dilution during growth are likely due to the following effects. 1) Atomic hydrogen "etches" a growing film, removing strained bonds that are in energetically unfavorable locations; 2) a high flux of atomic hydrogen promotes the surface diffusivity of adatoms so that they can move around to more energetically stable positions and form stronger bonds; 3) atomic hydrogen diffuses into the network, restructuring it and promoting a more stable structure. For the same reasons, sufficiently large hydrogen dilution induces the formation of microcrystalline Si. The enhancement of short range and long range order through hydrogen dilution has been observed in many deposition techniques, including PECVD (DC, RF, VHF and MW) and HW CVD; of course, the transitions from amorphous to microcrystalline structures occur at different dilution levels for different deposition techniques. It is believed that the more stable amorphous silicon is deposited under the conditions that are close to the microcrystalline formation [116].

The hydrogen dilution level for the transition from amorphous to microcrystalline silicon thin films depends on other deposition conditions also. At higher substrate temperatures (above 300 C), the transition from amorphous to microcrystalline state occurs at a higher H dilution; this effect is likely to be due to the low sticking coefficient of hydrogen on the surface [117]. At the low temperature side (below 250 C), it again takes a higher hydrogen dilution to reach the transition between amorphous to microcrystalline [117]; this effect is likely due to the low surface diffusivity of hydrogen during growth. When a-Si is deposited at a lower temperature with higher H dilution, more H is incorporated and the material has a wider bandgap. By following the edge of the transition curve (but staying on the amorphous side) while reducing the deposition temperature, widegap a-Si and single-junction a-Si n-i-p cells with 1.053 V open circuit voltage were deposited [118, 119]. It was also observed that materials deposited near the edge of microcrystalline formation show intermediate-range structural order [120].

## *3.7 Alloys & Doping*

As was discussed in Section 2.7, a-Si based alloys can be deposited using a gas mixture of $SiH_4$ with other gases such as $GeH_4$, $CH_4$, $O_2$ (or $NO_2$), and $NH_3$ for a-$SiGe_x$, a-$SiC_x$, a-$SiO_x$ and a-$SiN_x$, respectively. Among these alloys materials, a-SiGe has been explored extensively for photovoltaic applications as the narrow bandgap absorber. As we see from FIG. 10, the bandgap $E_G$ decreases with increasing Ge content. When $E_G$ is decreased to below 1.4 eV, the defect density becomes so high that the materials can no longer be used as the intrinsic layer for solar cells. Various approaches have been explored to make a-SiGe or a-Ge with low bandgap (below 1.3 eV) and low defect density [61]. Despite tremendous progress, device quality a-SiGe with low bandgap (below 1.3 eV) has not been demonstrated.

Another related aspect for a-SiGe deposition is the deposition uniformity. Due to the different dissociation rates of germane ($GeH_4$) and of silane ($SiH_4$) in an RF plasma, the film deposited near the gas inlet side the chamber has higher Ge content than the film near the exhaust. This non-uniformity makes it difficult to implement the process over large areas in manufacturing. By taking advantage of the approximately similar dissociation rate of $GeH_4$ and disilane ($Si_2H_6$), many research groups use a mixture of $GeH_4$ and $Si_2H_6$ for the fabrication of a-SiGe alloy and successfully obtained uniform film [52].

As discussed in Section 2.6, a-Si can be doped n-type by mixing phosphine ($PH_3$) with the gas mixture or doped p-type by mixing diborane ($B_2H_6$), $BF_3$, or trimethyl-boron (TMB, $B(CH_3)_3$) with the gas mixture during deposition. Due to the need for transparency in p-layers, which act as the "window" layer for sunlight, most cells have either μc-Si or a-SiC as the uppermost p-layer. Amorphous SiC p-layers are usually made using a mixture of $SiH_4$ and $CH_4$ strongly diluted in hydrogen [61]. The μc-Si p-layer is generally made in a PECVD process using high H dilution with high rf power at relatively low temperature. There have been suggestions that the optimum p-layer for a-Si solar cells is either nanocrystalline or is very close to the transition from amorphous to microcrystalline [121, 122]

## 4 Understanding a-Si *pin* cells

### *4.1 Electronic structure of a pin device*

Profiles showing electronic levels such as bandedges are an important tool in understanding device physics. FIG. 14 illustrates the profiles of the bandedge levels $E_C$ and $E_V$ for an a-Si:H based *pin* solar cell in the dark and under illumination. The figure is based on calculations using the AMPS-1D© computer program [123,124] and an idealized set of parameters to describe a-Si:H [125].* The electric field $F(x)$ within the device causes all electron level energies such as $E_C$ and $E_V$ to vary in space in the same way; for $E_C$ the expression is $eF(x) = \frac{\partial E_C(x)}{\partial x}$.

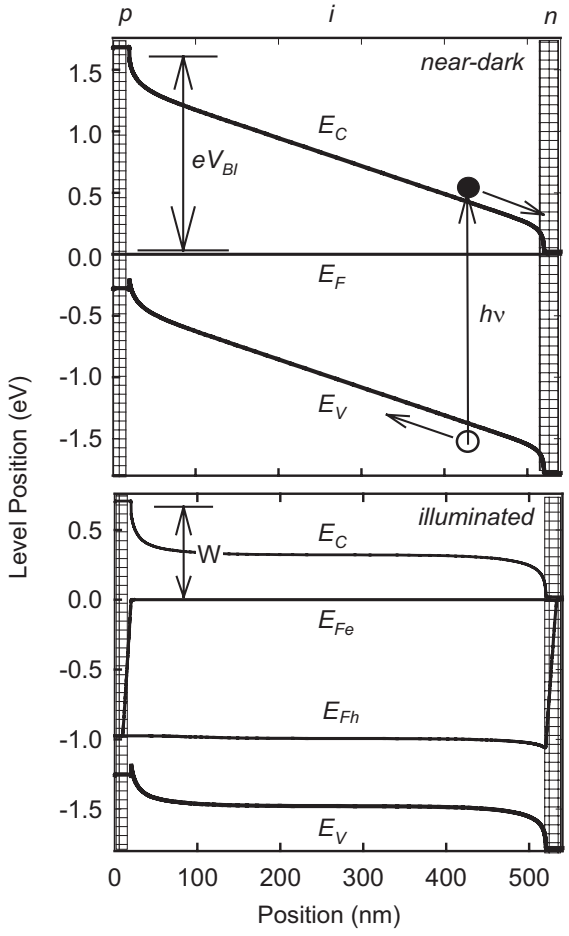


FIG. 14: Bandedge and Fermi-level profiles in a *pin* solar cell under open-circuit conditions. The open-circuit voltage is precisely the value of $E_{Fh}$ at the left interface ($x = 0$). The built-in potential $V_{bi}$ is illustrated. Note that the p-layer has a slightly (0.2 eV) larger bandgap than the i-layer; the calculation assumes symmetrical offsets of the valence and conduction bands at the *p/i* interface.

Where do these built-in electric fields come from? In isolation, *p*-type and *n*-type materials have very different Fermi energies; in the calculation of FIG. 14, we assumed that $E_F$ was 1.7 eV below $E_C$ for the *p*-layer, and was 0.05 eV below $E_C$ for the *n*-layer. When the *pin* device is assembled, these Fermi energies must be equalized to create thermal equilibrium. Electrons are donated from the *n*-layer to the *p*-layer, which generates a built-in electric field; while the level positions such as $E_C$ and $E_V$ now vary across the device, the Fermi energy itself is constant. The original difference in Fermi energies becomes the "built-in potential" $eV_{BI}$ across the device illustrated in the figure.* Electrons and holes that are generated by photon absorption will drift in the built-in electric field in the directions illustrated in FIG. 14.

The profiles of FIG. 14 were calculated assuming that the p-layer has an electrical bandgap of 2.0 eV, and that both the middle, intrinsic layer and the n-layer have bandgaps of 1.8 eV. The use of a wider bandgap *p*-layer, which is generally desirable in a-Si:H devices, can both increase $V_{BI}$ and reduce optical absorption in this layer. Because illumination generally enters amorphous silicon cells through the p-layer, this layer is also called the cell's "window layer."

## *4.2 Photocarrier drift in absorber layers*

The design of amorphous silicon based solar cells is strongly affected by how rapidly electron and hole photocarriers drift in an electric field. Ideally, electrons and holes should drift across the cell without interacting with each other, with the electrons ultimately being collected in the *n*-layer and holes in the *p*-layer. If, however, electrons and holes annihilate each other (in other words, if they "recombine" and generate heat), then there will be a loss of power from the cell. In this section, we illustrate one aspect of this loss process, which is the "collapse" of the internal electric field that occurs when the densities of photogenerated, drifting holes and electrons becomes sufficiently large.

FIG. 15 is a double logarithmic plot of the mean displacements *L(t)* for electrons and for holes as a function of the time since their generation by a photon. The results are presented for an electric field $F = 3\times10^4$ V/cm, which is about the right magnitude for a 500 nm intrinsic layer under short-circuit conditions. It is important to note that these displacements are proportional to electric field. They are based on laser-pulse "time-of-flight" measurements [41].

First consider the electron behavior. For the earlier times ($10^{-10}$ to $10^{-7}$ s), the displacement is simply proportional to the time, so we can just write the displacement as $L(t) = \mu_e F t$ . The parameter $\mu_\varepsilon$ is an electron mobility; it is about 1 $cm^2$/Vs, which is much lower than the mobility for electrons in crystal silicon (about 1000 $cm^2$/Vs near room-temperature). For longer times the electron displacement saturates at a value $L_{e,t} = 3\times10^{-3}$ cm. This effect is due to the capture of electrons by defects, which is called deep trapping.†

Let's briefly consider how these electron parameters affect the functioning of an amorphous silicon cell under short-circuit conditions. The main concern is the possible buildup of electric charge in the cell under solar illumination. If this "space-charge density" is

---

* We neglect interface dipoles.

† Quantitative study of deep-trapping involves normalizing of measured values for the drift-length $L_{e,t}$ by the electric field *E*, which yields the "deep-trapping mobility-lifetime product" $\mu\tau_{e,t} = L_{e,t}/E$ . $L_{e,t}$ varies inversely with the density of defects in undoped a-Si:H [23,49].

too large, then the electric field across the cell will "collapse." A collapsed field reduces the range over which the cell collects carriers, and reduces the cell's efficiency.

We start by determining the travel-time for an electron under short-circuit conditions. If the absorber (undoped) layer has a thickness $d$ = 500 nm, and a built-in potential $V_{bi}$ = 1.5 V across it (as for FIG. 14), then the electric field $E \approx V_{BI}/d$ in the dark is about $3\times10^4$ V/cm. Note that FIG. 15 was prepared using this value for $E$. An electron that is photogenerated near the middle of the absorber layer needs to travel about 250 nm to reach the *n*-layer (moving right across FIG. 14). Inspection of FIG. 15 shows that an electron's typical travel time $t_T$ across the absorber layer will be about 1 ns.

We can use this travel time of 1 ns to roughly estimate how much the total charge of electrons builds up under solar illumination. We write $\zeta = jt_T/2$, where $\sigma$ is the total electron space-charge in the absorber layer (per unit area of the cell); the factor of 2 implies that the current is carried equally by electrons and holes. For short-circuit conditions with $j_{sc} = 10$ mA/cm$^2$ we obtain $\zeta = 5\times10^{-12}$ C/cm$^2$. To find out whether the built-in electric field is affected by this space-charge density, we compare it to the built-in charge density $\sigma_{BI}$ near the doped-layers; $\sigma_{BI}$ is the charge which actually creates the built-in electric field. Using the standard expression for the charge-densities in a parallel plate capacitor, we estimate $\zeta_{BI} = \varepsilon\varepsilon_0 V_{BI}/d$ ($\varepsilon$ is the dielectric constant, and $\varepsilon_0$ is the "permittivity of the vacuum;" their product is about $10^{-10}$ C/Vm for silicon). We obtain $\zeta_{BI} \approx 3\times10^{-8}$ C/cm$^2$. Since $\zeta_{BI}$ is about 6000 times larger than the drifting space-charge $\sigma$ of electrons, we conclude that the drifting electrons don't significantly modify the built-in electric field.

We now turn to holes. Two aspects deserve particular attention. First, FIG. 15 shows that the drift of holes is *much* slower (orders of magnitude slower) than that of electrons. Second, and this also differs significantly from the properties of electrons, the displacement of holes is *not* proportional to time. Instead, the displacement *L(t)* for holes rises as a peculiar power-law with time:

$$L(t) = K(\mu_h/\nu)(\nu t)^{\alpha} E\,. \qquad (2)$$

where the numerical factor $K$ is about unity [126]. This type of *dispersive transport* [127] is actually rather common in non-crystalline semiconductors. The parameter $\alpha$ in the equation is the "dispersion parameter;" $\mu_h$ is the "microscopic mobility of holes," and $\nu$ is the "escape-frequency." Typical parameters for a-Si:H at room temperature are $\alpha = 0.52$, $\mu_h = 0.5$ cm$^2$/Vs, and $\nu = 8\times10^{10}$ s$^{-1}$ [41]. For

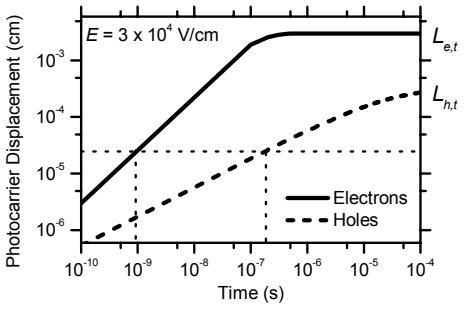


FIG. 15: Displacements (or drift lengths) of electron and hole photocarriers in a-Si:H as a function of time following generation at room-temperature [41]. Note that displacements are proportional to electric field. The saturation in the displacement for longer times (at $L_{e,t}$ and $L_{h,t}$) is due to deep-trapping of electrons and holes by defects. Dotted lines illustrate the time required to drift 250 nm.

a-Si:H, the dispersive transport for holes is explained by the "trapping" of holes in localized, exponential bandtail states just above the valence band (see FIG. 9). The dispersion parameter $\alpha$ is related to the valence bandtail width $\Delta E_V$ by the expression $\alpha = \left(k_B T / \Delta E_V\right)$, where $k_B T$ is the thermal energy ($k_B$ is Boltzmann's constant, and $T$ is the temperature in Kelvins). Electrons in a-Si:H also exhibit dispersive transport, but this is important only below room-temperature.

How much does the space-charge of holes build up under solar illumination conditions? The simple "travel-time" calculation that we used for electrons isn't valid for dispersive transport. Instead, we illustrate the effects of hole buildup using a computer simulation. In FIG. 16, we have presented the electric-field profiles $F(x)$ for four widely varying intensities of light; we assume that the light is absorbed uniformly throughout the absorber layer. At low intensities, the electric field is fairly uniform throughout the *i*-layer. As the illumination flux (and short-circuit current density) rises, the density of holes (and positive charge) build ups. At the highest intensity, the electric field "collapses" at the back side of cell (near the *n*-layer). In the next section we show how field-collapse influences the power generated by a cell. We have chosen to neglect other aspects of power-loss in the cell which apply when field collapse may be neglected [128,129], in particular for lower intensities.

## *4.3 Absorber Layer Design of a pin solar cell*

In this section we address the issues that determine the absorber (or "intrinsic") layer thickness. FIG. 17 illustrates a computer calculation showing how the output power of an a-Si based *pin* cell varies with intrinsic layer thickness. The differing curves represent results for monochromatic illumination using varying photon energies with the specified absorption coefficients. All the curves were calculated for the same photon flux. Such illumination conditions might be achieved experimentally using a laser whose photon energy could be tuned from 1.8 to 2.3 eV; sunlight, of course, presents a much more complex situation, as we

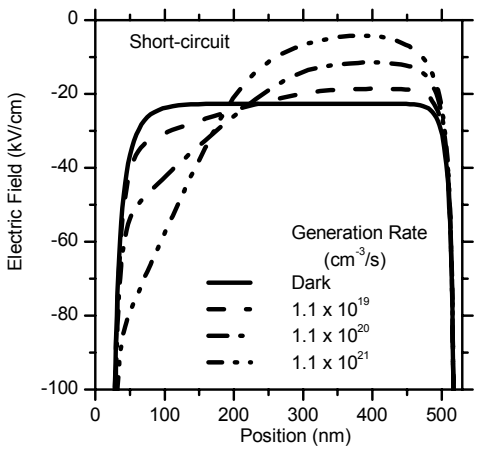


FIG. 16: Computer calculation (cf. FIG. 14) of the electric field profile of a *pin* solar cell for several illumination intensities; the cell is under short-circuit conditions. The illumination is uniformly absorbed ($\alpha = 5\times10^3$ cm$^{-1}$) throughout the *i*-layer, and the corresponding photogeneration rates are indicated. At low intensities, the electric field is nearly uniform across the intrinsic layer (which starts at a position 20 nm from the origin). As the intensities increase, the electric field collapses nearly to zero close to the *n*-layer, which starts at 520 nm. The field becomes stronger near the *p*-layer. At the highest intensity, the fully collected photocurrent density is 11.5 mA/cm$^2$, which is about the same as for solar illumination.

discuss in section 4.6.

We first discuss results for illumination through the *p*-layer (solid symbols in the figure). For intrinsic layers that are sufficiently thin, the power is proportional to the number of photons absorbed (i.e. to the product of the thickness *d* and the absorption coefficient $\alpha$). In this limit the fill-factors have nearly ideal values around 0.8.

As the thickness of the cell increases, the power saturates. First consider the behavior for strongly absorbed illumination ($\alpha$ = 100,000 $cm^{-1}$ – corresponding a photon energy of about 2.3 eV in FIG. 2). Power saturation occurs for thickness greater than 100 nm, which is the typical distance in which the photons are absorbed. Since thicker cells don't absorb much additional light, the power stops growing past this length.

For weakly absorbed illumination (5000 $cm^{-1}$ – corresponding to a photon energy of 1.8 eV in FIG. 2), power saturation occurs when the intrinsic layer is about 300 nm thick. This collection length [129] originates in the region where field collapse occurred in FIG. 16. The collapsed electric field is strongest near the *p*-layer, and weaker near the *n*-layer. It may not be evident, but recombination of electrons and holes occurs predominantly in the weak field regions. This effect can be roughly understood from the following argument. In regions with a field near zero, drift processes driven by electric fields do not determine the densities of photogenerated electrons and holes. Since the electrons and holes are being generated at the same rate, their densities are equal, and they build up under illumination until their rate *R* of recombination with each other matches the rate *G* of photogeneration *G* = *R*. It is worth noting that these conditions apply also to photoconductivity measurements that are made on isolated films of a particular material.

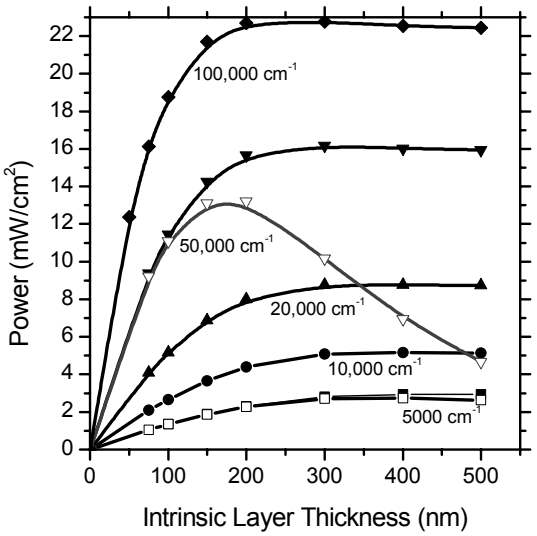


FIG. 17: Computer calculation of the power output from a *pin* solar cell as a function of intrinsic layer thickness. The differing curves indicate results for monochromatic illumination with absorption coefficients from 5,000 $cm^{-1}$ to 100,000 $cm^{-1}$; for typical a-Si:H, this range corresponds to a photon energy range from 1.8 to 2.5 eV (cf. FIG. 2). Solid symbols indicate illumination through the *p*-layer, and open symbols indicate illumination through the *n*-layer. Incident photon flux $2x10^{17}$ $cm^{-2}s^{-1}$; no back reflector.

The asymmetry in the drift of electrons and holes explains why amorphous silicon based *pin* solar cells are more efficient when illuminated through their *p*-layers. In FIG. 17 we have also shown (as open symbols) calculations for the power produced by cells that are illuminated through their *n*-layers. Consider first the results with weakly absorbed light (5000 $cm^{-1}$). In this case, the photogeneration of carriers is essentially uniform throughout the cells for all the thicknesses shown, and the cells don't "know" which side has been illuminated. Correspondingly, the power generation is essentially the same for illumination through the *p*-layer and through the *n*-layer.

Now consider more strongly absorbed light entering through the *n*-layer (50,000 $cm^{-1}$). When the cells are thinner than the absorption length (about 200 nm in this case), the photogeneration is essentially uniform. There is again no difference in the power generated for illumination through the *n* and *p* layers. However, for thicker cells, there is a pronounced drop in the power from the cell for illumination through the *n*-layer compared to illumination through the *p*-layer. The power falls because the holes, on average, must drift noticeably further to reach the *p*-layer than when they are generated by illumination through the *p*-layer. The electric charge of the slowly drifting holes builds up and "collapses" the electric field, leading to recombination and loss of power.

## *4.4 The Open-Circuit Voltage*

In FIG. 18 we present a summary of the open-circuit voltages ($V_{OC}$) for a-Si:H based solar cells from United Solar Systems Corp. as a function of the bandgap of the intrinsic absorber layer[130].* The measurements were done under standard solar illumination conditions. This graph is quite important to understanding the efficiencies of a-Si:H solar cells. For each photon absorbed, the solar cell delivers an energy $E = (FF)eV_{OC}$. The relation $V_{OC} = (E_G/e) - 0.80$ shows that most cells deliver a voltage that is 0.80 V below the bandgap. We can now roughly estimate the power delivered by a cell. For a 500 nm thick cell and a 1.75 eV bandgap, FIG. 2 shows that a typical photon absorbed by the cell under solar illumination actually carries nearly $h\nu \approx 2.5$ eV of energy. Since fill-factors are necessarily less than 1, the energy actually delivered by the cell can be no larger than 0.95 eV per photon – so over 60% of the absorbed energy must, alas, be lost in such a cell.

The simplicity of the dependence of $V_{OC}$ upon bandgap in FIG. 18 is only possible because open-circuit voltages depend only weakly on (i) the thickness of a-Si:H solar cells and (ii) the intensity of illumination. As a result, most details about the cells and measurement conditions are unimportant. For example, in the calculations of FIG. 17, the open-circuit voltage changed about 10% (from 0.9-1.0 V), while the output power varied from 1 to over 20 $mW/cm^2$.

Still another simplification applies to many cells. Most workers think that the very best open-circuit voltages in a-Si:H based cells have reached their "intrinsic limit." This means that these best values are not limited by the details of the *p* and *n*-type electrode layers [131], but are a fundamental property of the intrinsic layer.

We now give a short argument to explain how $V_{OC}$ is related to the energy profile of FIG. 14, and why $V_{OC}$ depends only weakly on thickness. The lower panel of FIG. 14 presents calculated open-circuit profiles of the bandedge levels $E_C$ and $E_V$ for a cell with uniformly

* We have assumed familiarity with the standard solar cell terminology of short-circuit current density $J_{SC}$, open-circuit voltage $V_{OC}$, and fill-factor *FF*. See chapter 3 for definitions of these terms.

absorbed illumination. No Fermi energy is shown in this lower panel because the cell is not in thermal equilibrium – it is exposed to light. Instead, electron and hole quasi-Fermi energies $E_{Fe}$ and $E_{Fh}$ are illustrated, which we'll define shortly. Notice that these quasi-Fermi energies merge together at the left edge of the *p*-layer, and again at the right edge of the *n*-layer; this merging means that an ordinary Fermi energy can be defined at these edges despite the presence of light. The product $eV_{OC}$ is the difference in these two Fermi levels, as illustrated in the figure. The center region of the cell is acting essentially as a solar battery!

We now define the electron and hole quasi-Fermi energies $E_{Fe}$ and $E_{Fh}$ [132,133]. For the electron quasi-Fermi energy $E_{Fe}$ we write:

$$n \equiv N_C \exp\left(-\left(E_C - E_{Fe}\right)\Big/ k_B T\right) , \tag{3}$$

where $n$ is the density of mobile electrons in the conduction band (ie. in the shaded region of the conduction band in FIG. 9). $N_C$ is the effective density ($cm^{-3}$) of these conduction band states. A similar expression accounts for the density of holes $p$ in terms of a distinct quasi-Ferm energy for holes $E_{Fh}$ and the effective density $N_V$ of valence band states.

Interestingly, in FIG. 14 the hole quasi-Fermi level is nearly constant across the cell, showing sizable variation only where it catches up to $E_{Fe}$ in the *n*-layer. Similarly, the electron quasi-Fermi level is constant except near the *p*-layer. This constancy means that the quasi-Fermi levels in the middle of the cell largely determine $V_{OC}$. The panel also shows that, in the middle of the cell, the bandedge potentials are essentially constant, and the electric field is very weak. As mentioned earlier, in such field-free regions the electron and hole photocarrier densities are equal and are determined by the condition that the recombination and photogeneration rates are matched. For cells which have attained the intrinsic limit, it is these fundamental processes which determine $V_{OC}$.

We now turn to the measured dependence of $V_{OC}$ upon the illumination intensity. Some recent measurements are presented in FIG. 18 [131]. The intensity was varied by using "neutral density" filters which attenuate all photon energies about the same. The short-circuit

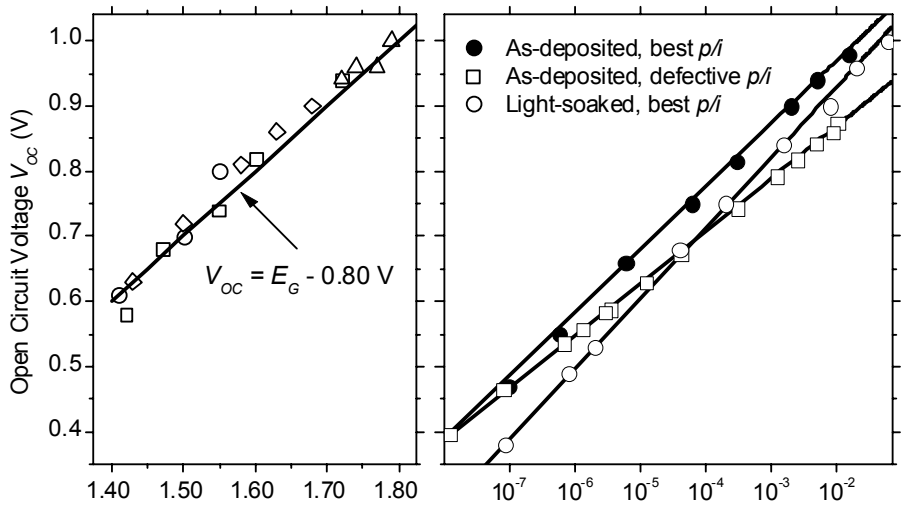


FIG. 18: (*left*) Open-circuit voltages for a-Si:H based solar cells as a function of optical bandgap [130]. The bandgap variation is due mostly to germanium incorporation. The measurements are from several laboratories; consult the reference for details. (*right*) Open-circuit voltage $V_{OC}$ vs short-circuit photocurrent density $J_{SC}$ for *nip* solar cells as reported by Pearce, *et al.* [131]. The short-circuit current density is proportional to the intensity of the illumination, which had a "white" spectrum similar to solar illumination.

current density $J_{SC}$ has been used as a "surrogate" for intensity based on their proportionality. Consider first the uppermost set of measurements ("as-deposited, best *p/i* interface"). The logarithmic dependence of $V_{OC}$ upon incident photon flux $F$ is typical of photodiodes [125,134]. For this sample, the slope of this dependence is determined by the defects; a second line in FIG. 18 ("light-soaked, best *p/i*") indicates how the dependence changed following an extended period of light-soaking. Interestingly, the difference in the two $V_{OC}$ vs. $\ln(J_{SC})$ lines is fairly small (about 0.02 V) under full solar illumination (about 10 mA/cm$^2$), where the effect of defects upon electron and hole motions is relatively unimportant. This fact partly explains why the dependence of $V_{OC}$ upon bandgap can be simple despite the wide variations in defect density for varying materials.

Our previous discussion concerns open-circuit voltages in the intrinsic limit. As might be expected, it is easy to fabricate a-Si:H solar cells with inferior open-circuit voltages. In FIG. 18, we have also shown the $V_{OC}$ vs. $\ln(J_{SC})$ relation [131] for a cell with an (intentionally) defective *p/i* interface (open squares). This cell was based on the same intrinsic material as the as-deposited cell with the best *p/i* interface (solid circles); the slope of the $V_{OC}$ vs. $\ln(J_{SC})$ relation is now noticeably reduced by the interface effect.

What aspect of non-ideal *p/i* interfaces leads to a reduction in $V_{OC}$? The physical mechanism through which a poor *p/i* interface diminishes $V_{OC}$ is the flow of photogenerated holes from the intrinsic layer (where they are generated) to the *p/i*-interface (where they recombine with electrons) [125]. The flow means that the hole quasi-Fermi-level has a gradient [133] near the *p/i* interface which reduces $V_{OC}$ below its intrinsic limit. You can just barely notice this gradient effect in FIG. 14.

The reason that this hole current flows is to balance an exactly equal current of electrons. The electrons are being thermionically emitted from the intrinsic layer and over the electrostatic barrier at the *p/i* interface. You can envision this thermionic process using the bottom panel of FIG. 14, which shows a barrier of $W = 0.6$ eV for electron emission from the quasi-Fermi level $E_{Fe}$ in the intrinsic material into the *p*-layer.

The best open-circuit voltages in substrate solar cells are achieved using a proprietary, boron-doped silicon film [135]. This material is generally referred to as microcrystalline, although extensive characterization of the type presented in FIG. 13 has not yet been published. The best open-circuit voltages in superstrate solar cells have been achieved using boron-doped amorphous silicon-carbon alloys (a-SiC:H:B). An indication of the subtlety required to achieve high open-circuit voltages is that cells using a-SiC:H:B *p*-layers also include a thin (<10 nm) "buffer layer" of undoped a-SiC:H between the *p*-layer and the intrinsic-layer of the cell [136,137,138]. The precise mechanism by which these buffer layers improve $V_{OC}$ is not conclusively established. We would speculate that the buffer layer impedes electron emission into the *p*-layer, in accordance with the "thermionic emission" model for *p/i* interface effects just described.

## *4.5 Optical design of a-Si:H Solar Cells*

In this section we briefly review the use of *back reflectors* and *substrate texturing,* which are optical design principles that are used to improve the power output of amorphous silicon based solar cells. The interested reader will find a more comprehensive treatment in the recent monograph of Schropp and Zeman [124].

Incorporating a back reflector increases the power output of solar cells. In FIG. 19, an ideal back reflector doubles the power output for weakly absorbed light (5000 cm$^{-1}$ in the figure); we are neglecting optical interference and "re-reflection" of light by the top of the cell, so the light passes through the cell twice, once on its way down to the reflector, and

again on its way back out the top. The back reflector has no effect on power output for strongly absorbed light (50,000 $cm^{-1}$ in the figure), since that light never "sees" the back-reflector. The effects of the back reflector are fairly complex when the thickness, absorption length of the illumination, and collection length for the holes are all comparable, which is what occurs for thicknesses in the range 100-300 nm with 50,000 $cm^{-1}$ illumination.

For weakly absorbed light, a back reflector for the simple planar structures just described increases power collection about two fold. Much larger improvements may be envisaged. The fundamental idea is "light trapping." An optical beam propagating inside a dielectric structure may be trapped by total internal reflection at the interface with air, which has a lower index of refraction than the dielectric. The principle is the same as that underlying the operation of optical fibers: an optical beam that enters the fiber at one end can travel kilometers without leaving the fiber. For solar cells, the light-trapping idea implies that a cell might fully absorb light even when its thickness is much less than the absorption length $1/\alpha$ for the light's wavelength.

Light-trapping is realized in amorphous silicon (and other) solar cells by using substrates that are "textured" or rough on the same scales as the principal wavelengths in solar illumination. The idea is that the random reflection/diffraction of light by the irregular, textured topography leads to internal reflection. Yablonovitch [139] showed that the maximum gain for such "statistical light trapping" in a textured film on an ideal reflector is $4n^2$, where $n$ is the index of refraction of the film; Yablonovitch's argument is fundamental, and not based on any particular form for texturing. For silicon films, with $n \sim 3.5$, the maximum predicted gain is nearly a factor of 50 (for light which is *very* weakly absorbed).

Experimentally, optical gains up to a factor ten have been reported from the use of textured substrates and weakly absorbed light [140,141]. In FIG. 19 we have presented measurements by Hegedus and Deng [141] of the "quantum efficiency" QE for a-Si:H solar cells made with several different textures and back reflectors. The quantum efficiency is defined as the ratio, at a specific photon energy, of the photocurrent density $j$ ($A/cm^2$) to the incident photon flux $f$:

$$QE = j/ef \quad . \tag{4}$$

Consider first the lowest of the curves (smooth substrate, no back reflector). For this sample, photons incident on the *p*-layer are either absorbed in the cell, or pass through the cell and leave it through the glass substrate. The rise of *QE* as the photon energy increases up to about 2.5 eV is due to the increase in absorption. A –1 V bias was applied, and the resulting electric field prevents the loss of photocarriers to recombination. Near 2.5 eV the quantum efficiency is nearly one: essentially all incident photons are absorbed, and nearly all the photocarriers generated are subsequently collected. The result is sensible. Inspection of FIG. 2 shows that the absorption coefficient is about $10^5$ $cm^{-1}$ at this energy, so that photons are absorbed within about 100 nm of the top surface of the a-Si:H. Since this length is much smaller than the sample thickness, essentially all photons are absorbed. Some photons are lost due to reflection from the glass and TCO interfaces, which accounts for most of the remaining losses.

For photon energies greater than 2.5 eV, the absorption coefficient continues to increase, so photons are absorbed within a few tens of nm of the top of the p-layer. A significant fraction of these photons is absorbed in the *p*-layer or the TCO; these photons do not contribute to the photocurrent, and so the QE declines for higher photon energies.

Now consider the data for the cell with an untextured substrate (0% haze), and a smooth Ag back reflector. For photon energies that are weakly absorbed (below 2.5 eV), the QE increases about twofold due to the back reflector; for strongly absorbed photons, there is little effect of the back reflector. These effects were just explained for the computer modeling of FIG. 19. Interestingly, the use of a textured back reflector further improves the QE. The textured reflector increases the typical angle between the paths of reflected photons and the axis normal to the substrate; this effect increases the typical path length of the reflected photon in the a-Si:H, as well as increasing the chance of reflection when a reflected photon arrives back at the top of the cell. The uppermost two curves, with the highest QE's, correspond to cells with textured substrates. For lower photon energies, the textured substrates further improve the QE, although certainly not to the maximum extent $4n^2$ calculated by Yablonovitch. Note also that substrate texturing also leads to a modest improvement of the QE in the blue spectral region (beyond 2.5 eV) due to a reduction in the front-surface reflectance of the cell.

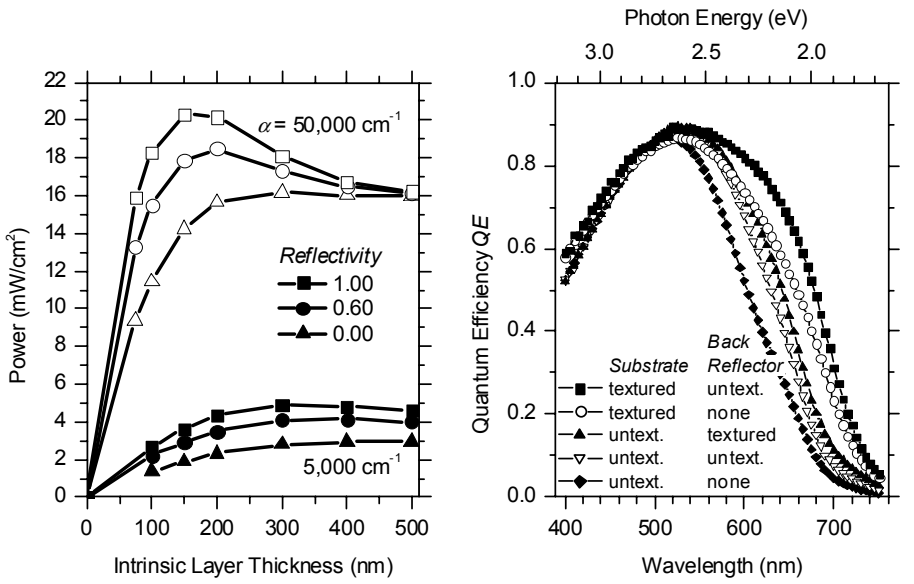


FIG. 19: (*left*) Computer calculation of the power output from a *pin* solar cell as a function of intrinsic layer thickness. The two sets of curves indicate results for monochromatic illumination (photon flux $2x10^{17}$ $cm^{-2}s^{-1}$) with absorption coefficients of 5000 $cm^{-1}$ (black symbols) and 50,000 $cm^{-1}$ (gray symbols). Results are shown for varying back reflectance; interference effects are neglected. (*right*) Quantum efficiency spectra for *nip* solar cells deposited under identical conditions, but with two differing substrate textures and differing back reflectors [141]. The sequence of layers in the structure was (TCO/p/i/n/TCO/glass/Ag). The Ag is the back-reflector material (when present); the TCO on top of the glass was either smooth or textured (14% haze).* Measured at -1 V bias.

* *Haze* is defined as the percentage of the light incident upon a film that is scattered incoherently. For transparent films, most of the remaining light is transmitted undeviated. Haze depends strongly upon the photon energy. The same value of haze can be obtained from films with quite different morphologies.

Roughly, the effect of back-reflectors and texturing for lower photon energies shown in FIG. 19 is to reduce the energy threshold for collection of an incident photon by about 0.2 eV. Using FIG. 2 one can estimate that this reduction in threshold increases the incident solar power absorbed by a 0.5 μm cell from 420 to 520 W/m$^2$. This estimate is broadly consistent with measurements showing an increase in short-circuit photocurrent under solar illumination of about 25% when textured substrates are used [140, 142, 143].

The implementations of texturing and back reflectors, as well as of a front "anti-reflection" coating to reduce the reflection, vary dramatically between superstrate and substrate cell designs. Superstrate cells usually incorporate a textured, transparent conductive oxide (TCO) coating on the transparent substrate (usually glass). There are many technologies for producing TCO layers from varying materials (typically $SnO_2$ or ZnO for a-Si based cells) and with varying texture and electrical properties. The semiconductor layers are then deposited onto the textured TCO. Plasma deposition of the p-layer onto a textured TCO can lead to difficulties: the oxide layer may be chemically "reduced," and achieving ideal properties for a thin p-layer can be difficult. Finally, the back reflector deposited on top of the semiconductor layers is often a two-layer structure: a thin TCO layer, followed by the reflective metal (typically Ag – for best reflectivity – or Al – for improved yield in production).

In substrate cells, the semiconductor layers are actually deposited onto the back reflector, which is again a two-layer structure starting with a textured silver or aluminum metallization and then a textured TCO [144]. Following deposition of the semiconductor layers, a top TCO layer is applied.

## *4.6 Cells under Solar Illumination*

In the previous few sections we have discussed the components of a-Si:H *pin* solar cell design. For monochromatic light and for a given intrinsic layer thickness, we have described the effects of the absorption length and the intensity, the effects of the slow (and dispersive) hole transport and the relatively rapid electron transport, and the use of back reflectors and texturing to enhance the photocurrents realized from weakly absorbed light. In this section we use essentially the same model for these effects as we have in previous sections, but extend it to a cell's operation under polychromatic, solar illumination. In addition, when we changed the bandgap, we left all other model parameters unchanged. This discussion continues in the following sections on multijunction (and multibandgap) cells.

In FIG. 20 we present calculations of the photovoltaic parameters $J_{SC}$, $FF$, $V_{OC}$, and solar conversion efficiency for *pin* solar cells of varying thickness and electrical bandgap. First note the increase in short-circuit current $J_{SC}$ as the bandgap is reduced (at constant thickness); this effect is due to the increase in optical absorption coefficients in the infrared as the bandgap is reduced (cf. FIG. 10). Also note that the short-circuit current depends only weakly upon thickness beyond the first 100 nm of thickness, which accounts for a substantial fraction of the total absorption. The decline of $V_{OC}$ with bandgap of course duplicates the experimental trend of FIG. 19. Interestingly, $V_{OC}$ remains essentially independent of thickness under solar illumination, despite the "front loading" of the photon absorption. On the other hand, the fill-factors under solar illumination are substantially larger than for uniform illumination. Finally, the differing trends of $V_{OC}$ and of $J_{SC}$ with bandgap conspire to determine a maximum efficiency of about 11.3% for a cell with a bandgap of 1.45 eV and a thickness greater than about 300 nm. While the neglect of deep levels is too idealized for these calculations to precisely describe the efficiencies, the calculations nonetheless indicate the principal trends of

changing the bandgap. They also suggest the strategy that has been used to achieve higher efficiencies. In particular, the effects of a decline in $V_{OC}$ with bandgap in single-junction cell can be avoided by building multijunction solar cells, as we describe in the next section.

## *4.7 Light Soaking Effects*

In FIG. 21 we illustrate the power output (standard solar illumination) for a series of cells of varying thickness prepared at United Solar Systems Corp. [14]. The cells are "substrate" type cells prepared on stainless steel. Results are shown both for the initial state of the cells and after 25,000 hours (degraded state). For the initial state of the cells, the power rises with thickness and saturates for thicknesses greater than about 400 nm, which is more or less consistent with the modeling presented in FIG. 17. In their degraded state, the cells reach their maximum power for a thickness around 200-300 nm; substantially thicker cells actually lose some power. As we have noted previously, the degradation effect is correlated with the increase in the defect density in a-Si:H as light-soaking proceeds. Although we did not include defects in the modeling presented in this section, one can understand the degradation effect qualitatively as due to hole trapping by light-induced defects instead of by valence bandtail states. We don't know whether the fact that the power "peaks" in the degraded state for thicknesses greater than about 300 nm is due to back reflection (cf. FIG. 19 ) or to

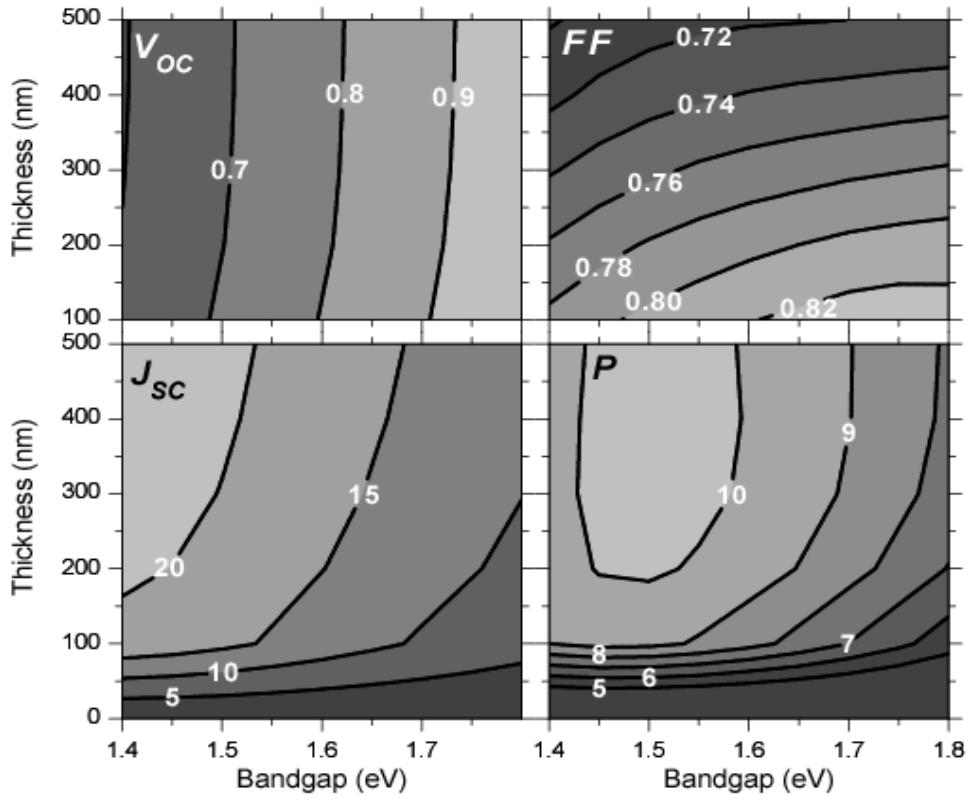


FIG. 20: Model calculations of the short-circuit current $J_{SC}$ (mA/cm$^2$), open-circuit Voltage $V_{OC}$,(V), fill factor *FF*, and power under AM1.5 illumination for a-Si:H based *pin* solar cells with varying intrinsic layer bandgaps and thicknesses. No back-reflector or texturing effects are included.

subtleties in the profile of light-induced defects.

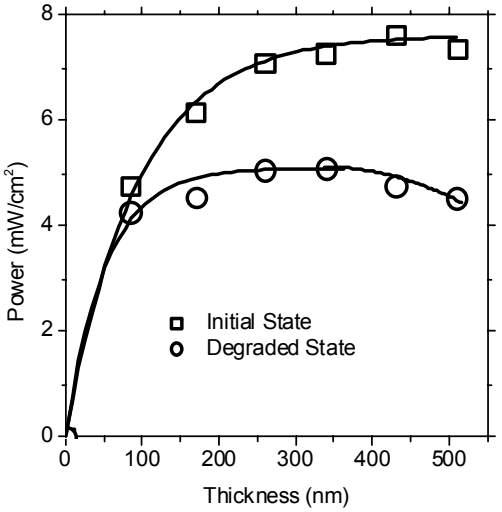


FIG. 21: Power output (standard solar illumination) for a series of *nip* solar cells with varying intrinsic layer thickness [14]. The degraded state was obtained by 30,000 hours of light soaking. The curves are guides only.

## Section 5 Multiple Junction Solar Cells

### *5.1 Advantages of multiple junction solar cells*

Amorphous silicon solar cells can be fabricated in a stacked structure to form multijunction solar cells. This strategy is particularly successful for amorphous materials, both because there is no need for lattice matching, as is required for crystalline heterojunctions, and also because the bandgap is readily adjusted by alloying. FIG. 4 illustrated the structure of a tandem cell with two junctions (ie. two *pin* photodiodes) in series. Multijunction, a-Si based solar cells can be fabricated with higher solar conversion efficiency than single-junction cells, and are presently used in most commercial cells.

The fundamental concept underlying multijunction solar cells is "spectrum splitting." Consider what happens if we deposit a second *pin* junction structure on top of a first one. The second structure "filters" the sunlight: photons absorbed in the top junction are of course removed from the light which reaches the bottom cell. We illustrated this filtering effect in FIG. 2, which shows that 500 nm of a-Si:H absorbs essentially all incident photons with energies greater than 2 eV, and passes photons with smaller energies. In practice, the thickness of the top *pin* junction is adjusted so that it filters out about half of the photons which would otherwise have been absorbed in the bottom *pin* junction.[*] Since the photons

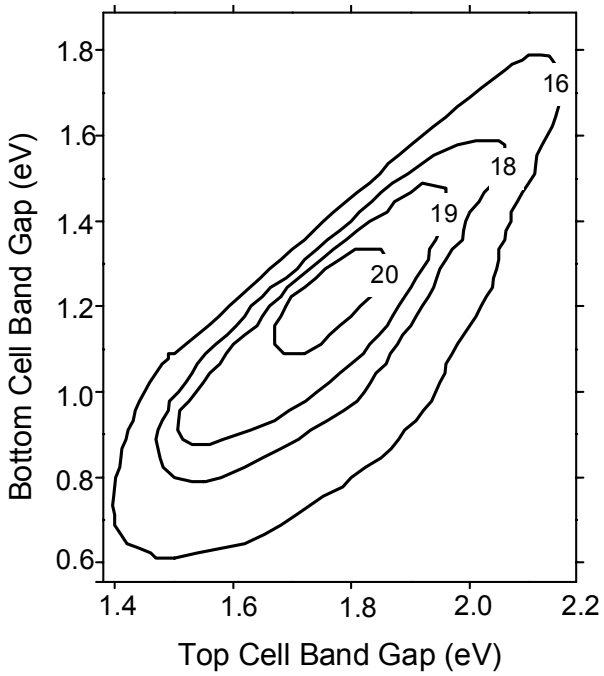


FIG. 22: Contour plot of constant solar conversion efficiency for a-Si based tandem solar cells for varying bandgaps $E_G$ of the top cell and bottom cell bandgap [146].

[*] We discuss only "two-terminal" multijunction cells in this chapter where a single electrical current flows through the series connected cells.

which are absorbed in the top junction have relatively large energies, we can use a material with a relatively large bandgap as the absorber for this junction, and we shall obtain a larger open-circuit voltage across the top junction than across the bottom junction. This is the "spectrum splitting" effect.

For specificity, consider a tandem cell which bases the bottom junction on material with a 1.55 eV electrical bandgap, and bases the top junction on material with 1.80 eV electrical bandgap material. In the absence of the top, 1.80 eV junction, the 1.55 eV junction might deliver about $J_{SC}$ =20 mA/cm$^2$ at an open-circuit voltage of 0.65 V. Assuming a fill-factor (FF) of 0.7, the power output will be 9.1 W/m$^2$. When assembled in tandem, the current through each junction is about half this value, but the open-circuit voltage will more than double ($V_{OC}$ = 0.65 + 0.90 = 1.55 V). The power output rises to 11.2 W/m$^2$ - for a 19% spectrum-splitting improvement over the single-junction device.

For ideal semiconductors arranged with optimal bandgaps, the maximum efficiencies for single, tandem, and triple-junction solar cells under concentrated sunlight are 31%, 50%, and 56%, respectively [145]. FIG. 22 shows the conversion efficiency contour plot calculated using an a-Si:H based computer model for two-junction tandem cells; the two axes are the . bandgaps for the top and bottom component cells [146, 147]. The best efficiency of over 20% occurs with a combination of a 1.8 eV intrinsic layer in the top *pin* junction and a 1.2 eV layer in the bottom. Of course, these model results have not yet been achieved in practice!

We can distinguish three reasons for improved efficiency in a-Si based multijunction cells over single-junction cells. The first is the spectrum splitting effect we have just described. Second, the *i*-layers in an optimized, multijunction cell are thinner than in single junction cells [148, 149]; as can be seen in FIG. 20, this "junction thinning" means that each individual junction will have a somewhat better fill factor than in the optimized single-junction device, and there will be less change from the initial to the stabilized efficiency of the cell. Third, a multijunction cell delivers its power at a higher operating voltage and lower operating current than a single-junction cell; the lower current reduces resistive losses as the current flows away from the junctions and into its load.

On the other hand, it is more challenging to fabricate multiple-junction solar cells than single-junction cells. The performance of a multijunction cell is more sensitive to the spectrum of the incident light due to the spectrum-splitting feature. This makes it even more critical to control the bandgaps and thicknesses of the individual layers. In addition, most multijunction cells incorporate a-SiGe alloys. These alloys are made using germane gas as the germanium source. Germane is several times more expensive than silane, and is highly toxic. Manufacturers need to implement strict safety procedures to handle these types of gases. Overall, the advantages and benefits of higher stabilized output power for multiple-junction cells do outweigh the difficulties in the fabrication.

## *5.2 Using Alloys for cells with different bandgaps*

As was mentioned in section 2.7, when a-Si is alloyed with other elements such as Ge, C, O, and N, amorphous alloy materials with different bandgaps can be made. This allows selection of appropriate bandgap combinations for high-efficiency solar cell fabrication. Since the bandgap of the a-SiGe alloy can be continuously adjusted between 1.7 and 1.1 eV when different amounts of Ge are incorporated in the alloy, it can be used as the low-bandgap bottom cell absorber layer for a multijunction solar cell. It is desirable to select a bandgap near 1.2 eV to achieve the maximum efficiency according to the contour plot in FIG. 22. Unfortunately, the optoelectronic quality of a-SiGe degrades rapidly when the a-SiGe

bandgap is reduced below 1.4 eV, and these materials have not proven useful for photovoltaic application.

FIG. 23 shows the *I-V* characteristics of a series of a-SiGe solar cells with different Ge concentrations in the i-layer (of constant thickness, and without a back reflector) [150]; the bandgaps are indicated in the legend. As the bandgap is reduced by incorporating more Ge in an i-layer, $V_{oc}$ goes down and $J_{sc}$ goes up (for a constant thickness), in agreement with trends for the calculations in FIG. 20. In FIG. 24, we have plotted the quantum efficiency curves of these same a-SiGe cells (along with one curve for a cell with a back reflector, and one curve for a cell with a microcrystalline Si *i*-layer). Consistent with the increase in $J_{SC}$, the quantum efficiency is increased for longer wavelengths (smaller photon energies) as the bandgap decreases

The fill factors of the cells also decrease as the bandgap decreases. This effect is due to the increased defect density in the alloyed materials. We have not included this important effect in the discussion previously. As the defect density in the *i*-layer increases, a given cell's performance will ultimately be dominated by the trapping of photocarriers on defects instead of by bandtail trapping. Roughly speaking, one can think of defect-trapping as reducing the "collection length" which determines the useful thickness of the intrinsic-layer (cf. FIG. 17). Naturally, one is principally interested in these effects for the "light-soaked" state achieved by operating cells.

When the Ge content is increased and the bandgap of a-SiGe is reduced to below 1.4 eV (see the *J-V* curve for the 1.37 eV cell in FIG. 23) , the FF deteriorates rapidly. In this case,

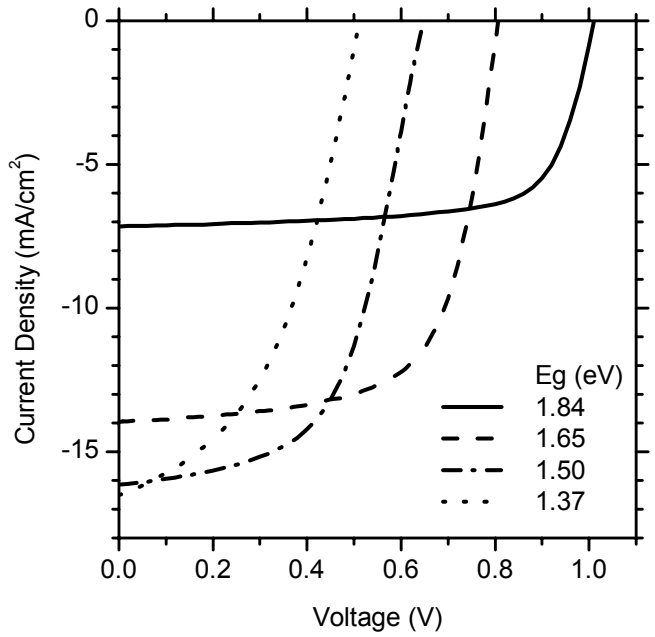


FIG. 23: Performance of a-Si and a-SiGe *nip* solar cells with different Ge concentrations in the i-layer ; the *i*-layer bandgaps are indicated in the legend. The fill factors for these cells are 0.70, 0.62, 0.55 and 0.43 for the cells with i-layers bandgaps of 1.84, 1.65, 1.50 and 1.37 eV, respectively. After [150].

the short circuit current density does not increase compared to the 1.50 eV cell even though more photons are absorbed. This lack of increase in $J_{sc}$ with further decrease in the bandgap occurs because the fraction of photocarriers that recombine has become more significant than the increase in the rate of photocarrier generation.

Similar to the deposition of a-Si, a-SiGe films and devices made with high hydrogen dilution show improved quality and light stability [151]. Optoelectronic properties of narrow bandgap a-SiGe material are nonetheless inferior than those of a-Si.

### Bandgap Grading

To enhance the fill factor of cells made using a-SiGe, bandgap *grading* is used to enhance the collection of holes [152,153]. In such a design, an asymmetric "V" shaped bandgap profile is created by adjusting the Ge content across the i-layer. Wider bandgap material lies closest to the *n* and *p* layers. The plane of narrowest bandgap lies closer to the *p*-layer (through which the photons enter into the device). Such a grading scheme allows more light to be absorbed near the p-layer so that "slower" holes do not have to travel far to get collected (see FIG. 10). Also, the tilting of the valence band assists holes generated in the middle or near the n-side of the i-layer to move toward the p-layer. With appropriate hydrogen dilution during growth and bandgap grading, a-SiGe cell can be made to generate up to 24.4 mA/cm$^2$ (27mA/cm$^2$ as the bottom cell in a triple cell) when a light enhancing back-reflector is used [154].

### a-SiC alloys

The bandgap of a-SiC can be adjusted between 1.7 and 2.2 eV, depending mainly on the C concentration [155]. After extensive research, most workers decided that a-SiC is not suitable for use as the i-layer of the uppermost cell in a multijunction structure. After light-soaking, a-SiC material that has an appreciable bandgap increase over a-Si is fairly defective and must be used in very thin layers; these layers do not absorb enough sunlight to be optimal. The wide bandgap material presently used in triple-junction cells is a-Si with a relatively

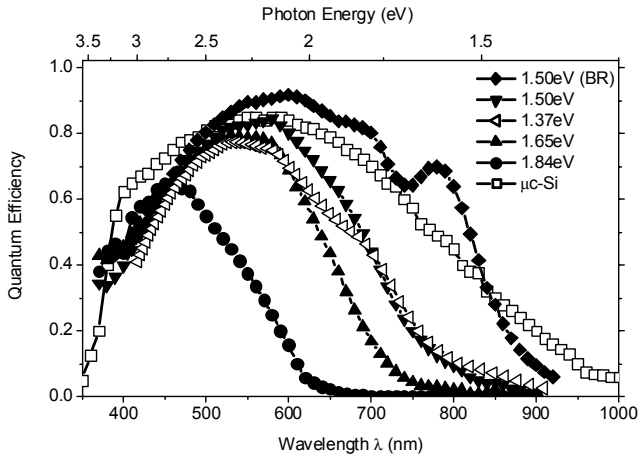


FIG. 24: Quantum efficiency (QE) spectra for a series of a-Si and a-SiGe based *pin* single junction solar cells with the indicated *i*-layer bandgaps. The 1.84 eV *i*-layer is a-Si; the 1.65, 1.50, and 1.37 eV *i*-layers are a-SiGe alloys. The abbreviation BR indicates a back-reflector; note the significant increase in the long-wavelength QE attributable to the textured back-reflector for the 1.50 eV cells. The QE spectrum μc-Si i-layer. Curve (f) is included here for a later discussion in Section 5.4. Spectra for the amorphous alloys are from [150], and for the microcrystalline structure is from [175].

higher concentration of H (achieved by using lower substrate temperature and H dilution) [8].

### *5.3 a-Si/a-SiGe tandem and a-Si/a-SiGe/a-SiGe triple junction solar cells*

Several types of multijunction solar cells have been used in a-Si photovoltaics. Dual-junction a-Si/a-Si (same bandgap tandem) solar cells have lower materials cost than tandem cells using a-SiGe, but have lower efficiencies than more advanced structures [156]. Dual-junction a-Si/a-SiGe cell and triple-junction a-Si/a-SiGe/a-SiGe cells, which use a spectrum-splitting approach to collect the sunlight, achieve higher conversion efficiencies. Some additional details and references may be found later in Table 4. Among these, a-Si(1.8eV)/a-SiGe(1.6eV)/a-SiGe(1.4eV) triple-junction solar cells have been used to obtain the most efficient a-Si based cells today [8]. FIG. 25 shows the structure of a triple-junction substrate cell* grown on stainless steel foil (SS); a superstrate-type tandem cell (glass substrate) was illustrated previously in FIG. 4. In both cases, light enters from the p-layer so that holes need to travel less distance to get collected than electrons. In the following, we will briefly describe the two designs and typical deposition processes that are most broadly used today.

In *nip* cells deposited on a stainless steel substrate, a reflective metal layer is deposited first on the substrate by sputtering or evaporation, followed by the sputter deposition of a ZnO buffer layer. Usually, silver is used as the reflective layer for research cells due to its high reflectivity, whereas aluminum is used in production due to difficulties with production yield for silver. The metal layer is deposited at high temperature (300-400 C); self segregation in the metal film forms the texture needed for light trapping. The sample is then moved into a RF PECVD deposition system for the deposition of semiconductor layers. The bottom *nip* with a an a-SiGe i-layer (1.4 to 1.5 eV bandgap) is deposited first. A second a-SiGe based

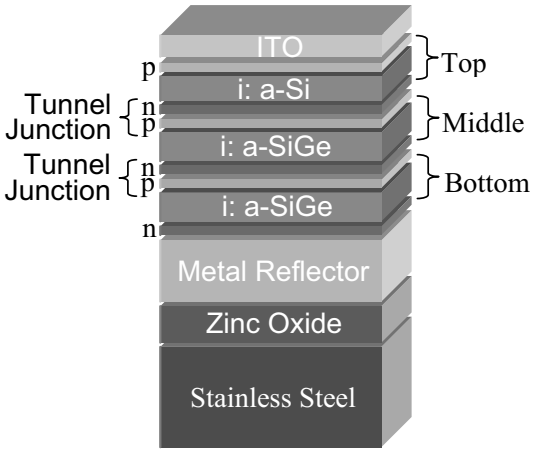


FIG. 25: Structure of triple-junction nip substrate type solar cells.

* Substrate and superstrate cells were illustrated in FIG. 3. The substrate-type cells are also called *nip* type cells, and superstrate-type cells are also called *pin* type cells, corresponding to the sequence in which the layers are deposited.

middle cell (1.6-1.65 eV *i*-layer bandgap) is then added. Finally, the top a-Si based cell (1.8-1.85 eV *i*-layer bandgap) is added; the intrinsic layer is made using high H dilution at relatively low temperature. An indium-tin-oxide (ITO) layer is deposited on top via evaporation or sputtering. This layer is approximately 70 nm thick, and serves as both the top electrode and an anti-reflection coating. Metal grids are evaporated or sputter deposited on top of ITO to further reduce contact resistance.

In *pin* superstrate cells deposited on glass, the glass substrate is first coated with a textured transparent conducting oxide, usually $SnO_2$ or ZnO, using one of several methods such as atmospheric pressure chemical vapor deposition (APCVD) [157, 158]. A *pin* top cell having an a-Si i-layer is then deposited, followed by the a-SiGe middle cell and finally the narrow bandgap a-SiGe bottom cell. The vertical structure is finished with the deposition of a ZnO buffer layer and metal reflector in the back.

### Current matching

In a triple-junction cell, the three component cells are stacked monolithically. Since these component cells are connected in series to form a two terminal device, the cell with minimum current density during operation will limit the total current of the triple-junction stack. Therefore, the current densities of each of the component cells need to be *matched* (made the same) at the maximum-power point for each cell in sunlight. The short-circuit currents $J_{SC}$ of the component cells are only a rough guide to this matching. For an a-Si/a-SiGe/a-SiGe triple-junction cell, the bottom a-SiGe cell usually has the lowest FF and the top a-Si cell usually has the highest FF. Therefore, the $J_{sc}$ of the bottom cell needs to be slightly greater than the $J_{sc}$ of the middle cell which in turn needs to be slightly greater than the $J_{sc}$ of the top cell. For an optimized triple-junction cell, the differences in $J_{sc}$ between the bottom and middle and between middle and top cells are each about 1 mA/cm$^2$. This is referred to as an intentional "mismatch" in the $J_{sc}$ values designed to match the cells at the operating point. To obtain highest stabilized solar cell efficiency, the triple cell needs to be designed, by adjusting the bandgaps and thicknesses of the component cell i-layers, such that the component cell currents are matched at the maximum power point in the light soaked state.

While adjusting for current matching, one needs to consider that the bottom cell benefits from the light enhancement from the back-reflector, as can be seen from FIG. 24, while the middle and top cells receive no benefit from the back-reflector.

### Tunnel junctions

Another area that needs attention in fabricating a multijunction solar cell are the *tunnel junctions* at the interfaces between adjacent *pin* cells. These interfaces lie between a *n*-type and *p*-type layers, and one might think that they would have electrical properties like classic *pn* junction diodes. However, researchers take advantage of one of the special properties of a-Si material that was discussed in section 2.6: dangling bonds are generated when doping is increased. Carriers that are trapped on defects on one side of the interface can move to traps on the other side simply by quantum mechanical tunneling. This process is sufficiently efficient that it "short-circuits" electrical transport involving the conduction band and valence band states [159]. For this reason, the doped layers at the tunnel junction, particularly the sublayers near the interface, are made with very high doping. The large density of dangling bonds permits the efficient recombination* (by tunneling) of holes from the cell below and electrons from the cell above, as illustrated in FIG. 25. This tunnel junction is reverse biased

* One can consider this as a neutralization process.

under normal operation; it must must generate negligible $V_{oc}$ and have negligible resistance and optical absorption. Use of μc-Si doped layers has proven critical to meeting these requirements [159].

### IV Measurement

In measuring the I-V performance of a multiple-junction, spectrum-splitting solar cell, researchers need to pay particular attention to the spectrum of the illuminating light [160]. A triple-junction cell for which the *pin* component cells are current-matched under the standard AM1.5 global spectrum may show poor performance under a different light source, e.g., a tungsten lamp. The triple-cell $J_{sc}$ is usually close to the $J_{sc}$ of the limiting component cell except when there is a large mismatch and the limiting cell has very low fill factor. The $V_{OC}$ of the triple cell is the sum of the $V_{oc}$'s of the component cells (and reduced by any photovoltages at the tunnel junctions). It should be noted here that the bottom component cell in a triple-stack generates only about 1/3 of the photocurrent that it would under full sunlight; therefore, its $V_{OC}$ is slightly smaller (usually by ~20 mV) than when it is exposed to the full sunlight. The middle cell will have about half the current that it would under the full sunlight. The fill factor of the triple cell depends sensitively on the fill factor of the limiting component cell and on the current mismatch among the component cells. A large mismatch leads to a higher triple-cell FF while on the other hand it also leads to a lower triple-cell current.

### Quantum Efficiency Measurements in Multijunction Cells

In measuring the quantum efficiency of a triple-junction solar cell, appropriate light bias and electrical bias need to be applied during the QE measurements [170, 171 or Chapter 17]. A direct QE measurement without these optical and electrical biases, just as one measures a single junction cell, would yield a "Λ" shaped curve, because a current can flow through the cell only if all of the component cells are illuminated simultaneously. When the QE of a specific component cell needs to be measured, say the middle cell, a DC bias light is illuminated on the cell through a filter that transmits only blue light and red light so that the top and bottom cells are illuminated. Under this condition, the middle cell current is limiting when the light through the monochromator is absorbed by the cell. Therefore, the current through the sample is that of the middle cell, i.e., the AC photo current at the monochromatic light which is absorbed in the middle cell. This ac photocurrent is modulated by an optical chopper, therefore can be easily detected using a lock-in amplifier (See Chapter 17).

The other two component cells can be measured in the same way except that different optical filters for the bias light need to be used. When the cells are measured without externally applied electrical voltage bias, the component cell being measured is actually under reverse bias, equal to the sum of the Voc of the other two component cells. In this case, the quantum efficiency curve would indicate the QE of the cell under reverse bias condition,

Table 4: Efficiency of small area solar cells fabricated in different laboratories.

| Structure | Initial η (%) | Stable η (%) | Organization | Ref. |
|---|---|---|---|---|
| a-Si/a-SiGe/a-SiGe | 15.2 | 13.0 | United Solar | 8 |
| a-Si/a-SiGe/a-SiGe | 11.7 | 11.0 | Fuji | 161 |
| a-Si/a-SiGe/a-SiGe | 12.5 | 10.7 | U. Toledo | 162 |
| a-Si/a-SiGe/a-SiGe | | 10.2 | Sharp | 163 |
| a-Si/a-SiGe | 11.6 | 10.6 | BP Solar | 164 |
| a-Si/a-SiGe | | 10.6 | Sanyo | 165 |
| a-Si/μc-Si | | 12.0 | U. Neuchatel | 166 |
| a-Si/μc-Si | 13.0 | 11.5 | Canon | 167 |
| a-Si/poly-Si/poly-Si | 12.3 | 11.5 | Kaneka | 168 |
| a-Si/a-SiGe/μc-Si | 11.4 | 10.7 | ECD | 169 |

which in most part is close to the QE under short circuit condition when the component cell FF is high. To measure the QE under short circuit current condition, electrical voltage needs to be externally applied to cancel out the voltage generated by the other component cells under the optical bias light. FIG. 26 shows the QE curves of a triple-junction solar cell measured using this method [162]. The short circuit current of component cells can be calculated by integrating the QE values with the AM1.5 light spectrum. The outer profile in FIG. 26 is obtained by adding the three component cell QE curves. Comparing the QE curves in FIG. 26 and FIG. 24, the middle cell QE is roughly the same as the difference curves (b) and (a) while the bottom cell QE is roughly the same as the difference between curves (e) and (b). The outer profile is roughly the same as curve (e) in the earlier figure.

### Matching Component Cells in Multijunction Designs

In matching component cell currents in the triple cell design, researchers usually take the following steps. Take the triple cell in FIG. 26 as an example. The design is largely dictated by the bottom a-SiGe component cell. If this component cell were fabricated on the back-reflector as a stand-alone single-junction cell, it would have a short circuit current around 23 mA/cm$^2$ and a QE curve similar to the one labeled "Total" in FIG. 26. In order to achieve current matching in the triple cell, a standalone, single-junction version of the middle a-SiGe component cell (without a back-reflector) needs to generate about 2/3 of the bottom cell's current. The bandgap and/or the thickness of the a-SiGe middle component cell's i-layer are then adjusted to accomplish this. Finally, the top component cell's thickness is adjusted to obtain 1/3 of the bottom cell's current (again, without a back reflector). In this way, all three cells would have the same current when they are stacked in series.

In FIG. 26, the long-wavelength behavior of the QE curves for each of the component cells is determined by the component cell's i-layer thickness and bandgap, and (for the bottom component cell) by the back-reflector performance. However, the short-wavelength behaviors for the middle and bottom component cell's QE curves are largely determined by the thicknesses and bandgaps of the top and middle cells, respectively, since these component

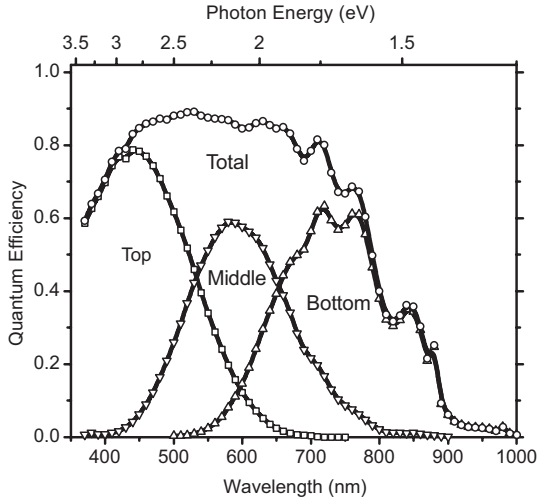


Short-circuit Current $J_{SC}$ (mA/cm$^2$)

| | AM1.5 | Xenon |
|---|---|---|
| Top | 6.87 | 7.19 |
| Middle | 7.84 | 7.98 |
| Bottom | 8.62 | 7.34 |
| Total | 23.03 | 22.51 |

FIG. 26: Quantum efficiency curves of component cells of a typical triple-junction solar cell. The table indicates the short-circuit current densities $J_{SC}$ for the component cells measured for AM1.5 illumination and with a xenon illuminator [162].

cells act as filters for the shorter wavelength (higher energy) photons. The short-wavelength behavior of QE for the top cell is sensitive to the absorption of ITO and top cell p-layer as well as the loss of electrons diffused back to the p-layer and get trapped.

### High efficiency multiple-junction solar cells

Table 4 above lists some properties for multiple-junction solar cells fabricated in selected laboratories around the world. The degradation of multiple-junction solar cells is usually in the range of 10-20% while the degradation of single-junction solar cells is usually in the range of 20-40%. These percentages apply to the cell's properties after 1000 hours of light soaking under 1 sun light intensity at 50 C, which is the standard protocol used for gauging light degradation today. The degradation of triple cells is smaller because 1) the i-layers are thinner, and 2) each i-layer absorbs only 1/3 of the total current, therefore having less photo-generated recombination in the i-layer. As one can see from the Table, the highest stabilized cell efficiency is 13.0% for a the triple-junction device structure made at United Solar Systems Corp.. Table 4 also includes the best solar cells made using μc-Si as a component cell. The cell with highest stable efficiency so far using a-Si/μc-Si tandem structure is 12% for a cell made at Univ. of Neuchatel using VHF plasma deposition.

## *5.4 Microcrystalline Silicon Solar Cells*

Microcrystalline silicon (μc-Si) has been studied extensively for three decades [172] and has been used for doped layers in a-Si solar cells for over 15 years [135,173]. Due to the difficulties in passivating the defects located at the grain boundaries, μc-Si was not actively considered as an intrinsic layer in the pin or nip type solar cells until 1992, when Faraji, *et al.* [174] and Meier, *et al.* [175] reported the fabrication of μc-Si based *pin* solar cells using VHF PECVD. Since then, μc-Si and poly-Si solar cells have been fabricated by a number of research groups [176, 177, 167, 178].

A QE curve for such a μc-Si based cell was presented FIG. 24. One can see that the μc-Si has a larger QE than the a-Si and a-SiGe cells at longer wavelengths (>850 nm). The total photocurrent generated from a μc-Si cell has reached 26 mA/cm$^2$ [175, 177]. Therefore, such cells are suitable for use as the bottom cell of a multijunction cell with a-Si based cells as the top cell. The advantages of using μc-Si as the narrow bandgap cell instead of a-SiGe are: 1) the higher QE in the long wavelength region; 2) negligible light induced degradation; 3) reduced materials cost, since μc-Si can be made using $SiH_4$, which is a relatively low-cost gas compared to $GeH_4$; and 4) μc-Si cells can be made with high FF. On the other hand, the concerns associated with using μc-Si compared to a-SiGe bottom cell are 1) μc-Si cells require much thicker i-layers (several microns thick) to absorb the sunlight; this is an effect of the lower interband absorption coefficients in (indirect bandgap) crystals compared to amorphous semiconductors; 2) the deposition rate for μc-Si material is generally low, so that a much longer time is needed to complete the deposition of a thick μc-Si layer than is needed for an a-SiGe layer; and 3) μc-Si solar cells have lower $V_{OC}$ (around 0.53 V) than do a-SiGe cells yielding the same $J_{SC}$.

Beside VHF technique, μc-Si has also been deposited using other high deposition rate methods such as hot-wire CVD [179], GasJet/MW deposition [180] and high power/high pressure RF deposition [181]. A typical deposition rate for an a-SiGe i-layer is 0.3 nm/s; to complete a μc-Si cell with comparable deposition time, one would need to deposit μc-Si with at least ~20-30 Å/s deposition rate so that it would not be rate-limiting during production.

## *5.5 Micromorph and other μc-Si based multijunction cells*

Meier, *et al.* [182] used an a-Si *pin* junction as the top component cell and a μc-Si *pin* as the bottom component cell for a-Si/μc-Si tandem cells; they named these cells "Micromorph" devices. The 1.7eV/1.1eV bandgaps for the top/bottom cell provide a nearly ideal bandgap pair for tandem cells (see contour diagram in FIG. 22 above).

In order for an a-Si/μc-Si tandem cell to have comparable performance as a-Si/a-SiGe cell, the bottom cell μc-Si must have at least 26 mA/cm$^2$ current density. Since μc-Si has an indirect bandgap, generating such a high current requires the μc-Si layer to be several microns thick. In addition, advanced light enhancement schemes need to be used. In order to maintain current matching in a micromorph cell , the top a-Si component cell must generate 13 mA/cm$^2$ (ie. half the current for a standalone μc-Si). In addition, this a-Si cell needs to be stable under light so that the tandem cell could be stable.

Two approaches were taken to accomplish this [183,184]. First, the a-Si i-layer is made at a relatively higher temperature, so that there is a lower H concentration (and a reduced bandgap, ~1.65 eV). Secondly, a semi-reflective layer was inserted at the tunnel junction between the top and bottom cell. This semi-reflective layer permitted current matching (enhancing the top component cell current at the expense of the bottom cell). With these two approaches, 13 mA/cm$^2$ $J_{SC}$ was obtained from the top cell with a 3000 A thick a-Si layer. Innovative approaches need to be taken to further increase the current beyond the present level. With the micromorph tandem design, solar cells with 11-12% stable efficiency have been fabricated [167,184].

One can also combine a-Si and μc-Si cells to fabricate a-Si/μc-Si/μc-Si triple cells. Such a design would relax the stringent requirement on the a-Si top cell due to current matching since it now only needs to generate 1/3 of the bottom cell current. However, the presently low $V_{OC}$ of a μc-Si cell militates against the triple junction design.

Still another approach a triple junction cell is to combine a 1.8eV a-Si top cell, a 1.6 eV a-SiGe middle cell, and a 1.1 eV μc-Si bottom cell [169]. Such a cell design would have the advantages of a thinner and more stable top cell than for a micromorph tandem cell, would have better long wavelength collection, and reduced consumption of (expensive) $GeH_4$ gas compared with an all-amorphous, a-Si/a-SiGe/a-SiGe triple junction cell.

## Section 6 Module Manufacturing

Although the stabilized conversion efficiency of a-Si based solar cells is presently lower than those of several other types of solar cells, a-Si based PV products are highly attractive for terrestrial applications since they can be produced using low-cost manufacturing methods. The a-Si PV products are environmentally friendly. They are made mostly using silicon, which is abundant on earth. In addition, the a-Si PV products can be made lightweight, flexible and radiation resistant. These make them highly desirable for portable power applications as well as for space power applications. Furthermore, the fact that a-Si products have higher stabilized power output at higher temperature makes these products more desirable in warm weather environment.

During the past ten years, there has been a rapid increase in the worldwide a-Si production. At this time in 2002, the total worldwide a-Si production capacity exceeds 85 MW/yr, including about 30 MW at United Solar Systems Corp.(USA), 20 MW at Kaneka Corp. (Japan), 10 MW at BP Solar, Inc. (USA), 10 MW at Canon (Japan), 6 MW at Sanyo (Japan), 3 MW at EPV (USA), 2MW at Sovlux (Russia) and several 1 MW plants in various companies in different parts of the world.

These production facilities can be roughly divided into two major categories: those with substrate-type a-Si PV products and those with superstrate type a-Si PV products. To transfer small area R&D developments into any type of large-scale manufacturing, key issues including uniform deposition over large areas, process gas utilization, deposition rate, production throughput, process reproducibility, machine maintainability and serviceability, process automation and production yield must be addressed.

For a large-scale production line, in-line processes have been used by all major manufacturers. In the following, we use the production process at United Solar as the example for the substrate type process and that at BP Solar as the example for the superstrate type process.

### *Continuous Roll-to-Roll Manufacturing on Stainless Steel Substrates*

The continuous, "roll-to-roll" a-Si PV manufacturing process was developed by Energy Conversion Devices, Inc. (ECD) and has been used by ECD's PV joint ventures and partners, (United Solar, Sovlux, and Canon) [185, 186,187]. Roll-to-roll refers to the process whereby a "roll" of flexible stainless steel (SS) is unrolled and fed into the manufacturing process, and then the stainless steel is again "rolled up" after a manufacturing step has been completed. The production process can be separated into two distinct parts: the front end coating process and the back-end module assembly process.

The front-end process consists of four continuous, roll-to-roll steps in separate machines: (i) substrate washing, (ii) sputter deposition of the back-reflector, (iii) a-Si and μc-Si semiconductor deposition, and (iv) ITO top electrode deposition. Rolls of magnetic stainless steel web, typically 125 μm thick, 0.35 m wide and 750 m long, are guided through these roll-to-roll machines by magnetic rollers. The roll is unwound from a modular "pay-off" chamber on one side and wound up in a modular "take-up" chamber on the other side. FIG. 27 is a photo of front-end facilities at an ECD designed 2MW plant, operated by Sovlux, and showing all four roll-to-roll machines.

In the roll-to-roll washing machine, the stainless steel web is guided through ultrasonic detergent cleaning stations with spinning brushes rubbing the surface, multiple deionized

water rinse baths, and an infrared drying chamber. An oil-free, particle-free, clean stainless steel roll is then wound up with protective interleaf.

The roll is then unloaded from the take-up chamber of the wash machine and loaded into the pay-off chamber of back-reflector sputter machine. In this machine, the SS web is pulled through several DC magnetron sputter deposition zones with metal targets (Al, Ag or other alloys) for the reflective layer and ZnO targets for the deposition of ZnO buffer layer. The substrate is maintained at elevated temperature during sputtering so that the metal films develop a texture useful for optical enhancement [186, 188].

The roll is then loaded into the RF PECVD machine for the continuous roll-to-roll deposition of 9 layers of semiconductors (nip/nip/nip) as well as all of the buffer layers on both side of a-SiGe absorber layers. The deposition of the different layers occurs sequentially but in a single pass. Innovative "gas-gate" design allows the manufacturer to isolate the feedstock gases in different chambers and to prevent cross-contamination, while at the same time the web passes through the sequence of chambes continuously. The gas-gate utilizes laminar gas flow to effectively isolate the gases in adjacent chambers.

After the semiconductor deposition, the roll is then loaded into TCO deposition machine, which uses either reactive evaporation of indium in oxygen ambient, or sputtering from an indium-tin-oxide (ITO) target in an argon atmosphere. The thickness of the ITO is carefully monitored to achieve antireflection properties.

The four roll-to-roll steps are currently not integrated into one machine. This design reflects the different pressure ranges for the four machines: atmospheric pressure for the washing, a few mTorr for Back-reflector sputtering, around 1 Torr for PECVD, and a few mTorr for TCO sputtering.

At this point, the stainless steel roll is a giant solar cell, 700 m long, which needs to be connected to get higher voltage for the modules. The semi-automatic back-end process for cell interconnect and module assembly includes the following steps. The roll of TCO coated

FIG. 27: A photograph of the Energy Conversion Devices, Inc. 2 MW plant showing all four front-end roll-to-roll machines for washing, back-reflector sputter deposition, PECVD deposition (right hand side) and TCO deposition. After Izu, *et al.* [186].

a-Si solar cells is first cut into slabs of selected sizes with a slab cutter. Etching paste is then applied to the edge of the slab and activated through a belt furnace to remove ITO around the perimeter of the slab and to define effective solar cell area. Selected small samples (coupons) are collected throughout the run for quality-assurance and quality control (QA/QC) evaluation. The standard slabs then go through a shunt passivation process in an electrolyte bath to remove and isolate small shunts by converting the TCO at the shunting point into an insulator [189]. The grids, either carbon paste or copper wire coated with carbon paste, are then applied to the slab to complete a strip cell, which is a big cell that generates ~2.3 V voltage and ~2A current. Different numbers of strip cells, depending on the module specification, are connected together in series with the grids/bus-bar of one strip cell connected to stainless steel substrate (the opposite electrode) of the neighboring strip cell. By-pass diodes are also installed at this step for the strip cell protection. The connected cells are then covered with ethyl vinyl ethylene (EVA) and Tefzel, which are transparent encapsulating layers, and cured in an oven for appropriate time for lamination, which is then followed by selected module framing.

Despite the need for relatively labor-intensive module assembly process at the moment, the continuous roll-to-roll production of a-Si solar panels on SS substrate has a number of advantages. The product is lightweight and flexible. The front-end production process requires low maintenance and can be easily scaled up. The coated SS roll may be cut into slabs of various sizes to make different products. For example, small sizes are suitable as battery charger, and large sizes as metal roof shingles (more than 5 meters long). A high production yield can be maintained. The disadvantage is the need for labor-intensive cutting, gridding and interconnecting individual cells to create a module.

In the process at Iowa Thin Films, Inc., a flexible Kapton* substrate is used. The cell interconnect is achieved by laser scribing, similar to the process at BP Solar for superstrate type solar cells, as to be described below.

## *6.2 a-Si module production on glass superstrate*

The manufacturing of a-Si solar panels on glass superstrates is being developed by several companies including BP Solar, Inc. (USA), Energy Photovoltaics, Inc. (USA), and Phototronics Solartechnik GmbH (Germany) [190]. A typical process is that of BP Solar's 10MW plant (TF1) in Toano, Virginia, (USA) [191].

The process begins with large sheets of "float" glass, 3 mm thick with a typical size of 1 m by 0.5 m. A textured tin oxide TCO layer is deposited using an atmospheric pressure chemical vapor deposition (APCVD) process either at the glass supplier's plant or at the PV plant. The substrate is edge polished and cleaned before silver frits are applied as bus bars and cured in a belt furnace. This TCO layer is "scribed" by a laser into strips about 9mm wide. The substrates are then loaded in the PECVD machine for the deposition of the six semiconductor layers for an a-Si/a-SiGe *pin*/*pin* tandem structure. The semiconductor deposition is followed by the deposition of a ZnO buffer layer. Another laser scribing is done at this point adjacent to the first scribe lines. This second scribing is done at a lower laser power so that, while the ZnO and a-Si layers are scribed, the underlying tin oxide layer remains intact. An aluminum layer is sputter-deposited as the back-reflector and back contact. A third scribing of the Al adjacent to the second completes the interconnection of neighboring cells in series, as shown in FIG. 28. A fourth, high-power laser scribing around the perimeter of the solar panel isolates the active area from the edges. The panel is then finished by

* ®Registered trademark of the Dupont Corporation.

bonding a second glass plate onto the cells with EVA. This second piece of glass is needed for encapsulation, which unfortunately adds weight and cost to the module.

## 6.3 Manufacturing Cost, Safety and Other Issues

An important aspect for any manufacturing process is cost., which generally consist mostly of raw materials, labor, capital depreciation of the machines, and administration. The overall production cost per unit of product is reduced as the production volume goes up. At a high production volume, perhaps 100 peak megawatts/year 100 $MW_p$/yr (under illumination yielding peak power production), the cost is expected to be lower than $1/Wp. At the present time, for a-Si modules intended for outdoor use for extended time, the major costs are the module framing, encapsulation, and the substrates (glass or SS). As an example, for the materials cost, the current breakdown at BP Solar's 10MW plant is: 33% for framing and packaging, 38% for TCO/glass, 17% for germane, 7% for encapsulation and 5% for silane and other feedstocks [63].

Another important aspect with regard to a-Si PV manufacturing is the plant safety. Although there is no toxic material in the final product, the manufacturing processes do involve toxic and pyrophoric gasses such as germane, phosphine, trimethylboron, silane, hydrogen etc. Amorphous Si PV manufacturers, who have learned and borrowed heavily from the safety procedures developed by the integrated circuit industry, use a variety of methods to improve safety of workers. Toxic gases are diluted in hydrogen or silane to 1-20%. Gas cylinders are installed outside the building or in fireproof gas cabinets. Toxic gas monitors are installed throughout the plants. Automatic gas isolation and operation shutdowns are implemented. These, among other safety procedures, ensure safe operations in these plants.

The solar conversion efficiency of production modules is generally lower than the efficiency of research & development (R&D) scale, small area solar cells since production processes are more restrained by cost reductions. The differences in efficiency are mostly from the TCO performance, semiconductor material quality, deposition uniformity, encapsulation loss, bus bar shadow loss and electrical loss, and small shunts. Rech, *et al*. provided a detailed analysis in the efficiency differences between R&D and manufacturing at Phototronics, Germany [192].

## 6.4 Module performance

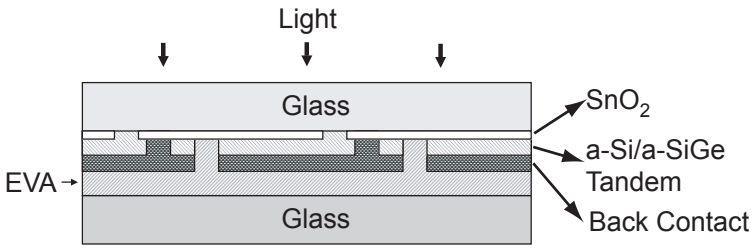


FIG. 28: Cell interconnection of superstrate type solar cells, used at BP Solar..

Two aspects of PV modules are generally evaluated: maximum solar conversion efficiency and environmental stability. Table 5 lists PV modules produced in selected organizations around the world; the table separately lists modules made in R&D type machines (area about $0.1m^2$), and large-area modules (area 0.4 $m^2$ or greater), mostly produced from production lines. At this time in 2002, large-area modules, with approximately 8% stable efficiency, are manufactured at United Solar and BP Solar and are commercially available in large quantities.

Photovoltaic modules are also evaluated through various environmental tests, as listed in UL, IEC and IEEE standard testing procedures (See Chapter 17 for more on module testing). These tests generally include thermal cycles between –40C to 90C; humidity freeze cycles between –40 to 85C at 85% humidity; hail impact; wet hi-pot test and light soaking. PV modules that are sold for commercial use have generally been qualified by these testing programs.

Table 5: Stabilized efficiency of a-Si PV modules manufactured by various companies.

| Structure | Stable $\eta$ (%) | Size ($m^2$) | Company | Reference |
|---|---|---|---|---|
| **R&D modules** | | | | |
| a-Si/a-SiGe/a-SiGe | 10.2 | 0.09 | United Solar | 187 |
| a-Si/a-SiGe | 9.1 | 0.08 | BP Solar | 164 |
| a-Si/a-SiGe | 9.5 | 0.12 | Sanyo | 193 |
| **Large-area Modules** | | | | |
| a-Si/a-SiGe | 9.3 | 0.52 | Sanyo | 194 |
| a-Si/a-SiGe/a-SiGe | 9.0 | 0.32 | Fuji | 161 |
| a-Si/a-SiGe | 8.1 | 0.36 | BP Solar | |
| a-Si/a-SiGe/a-SiGe | 7.9 | 0.45 | United Solar | |
| a-Si/a-Si/a-SiGe | 7.8 | 0.39 | ECD | 186 |
| a-Si/poly-Si | 10.0 | 0.37 | Kaneka | 195 |

## Section 7 Conclusions and Future Projections

### *7.1 Status and Competitiveness of a-Si Photovoltaics*

Over the last quarter of a century, significant progress has been made in the understanding of properties and of deposition processes for a-Si based materials and solar cells. There have been impressive achievements both in increasing the conversion efficiency of solar cells and in the reducing the cost of fabrication. In 1997, a-Si based solar cells with 15.2% initial efficiency and 13% stable efficiency were demonstrated [8]. The manufacturing volume of a-Si solar modules has increased more than 10 fold over the past ten years, and capacity is presently more than 75 $MW_p$/yr. There are now seven a-Si PV manufacturers with production capacity of 2 $MW_p$/yr or more.

In the pipeline for the future, significant progress has been made in the development of rapid deposition processes (> 0.5 nm/s) that achieve essentially the same quality as the present, slow processes, as discussed in Section 3. As rapid deposition and high gas utilization processes are incorporated into production, further cost reduction will be achieved.

Additionally, the use of microcrystalline silicon as the narrow bandgap absorber layer in an a-Si based tandem solar cell has been demonstrated, and cells exceeding 12% conversion efficiency (stabilized) have been produced in different labs. The cells incorporating μc-Si show superior light stability over extended light soaking.

Amorphous Si based PV technology is unique compared with other PV technologies. a-Si absorbs sunlight more strongly than c-Si and poly-Si because it is amorphous; the selection rules that weaken absorption in c-Si (an "indirect bandgap" semiconductor) do not apply to a-Si. A rather thin layer of a-Si is sufficient to absorb sunlight. a-Si can be made at a low temperature on inexpensive substrates. The product is made through a low-cost process. The energy payback time (the time required for an a-Si module to generate the energy used in its production) was estimated as 1-2 years in 1989, and has probably shrunk substantially since then [196]. One expects that the cost will continue to decline as the production volume is increased. When deposited on selected substrates, the product can be made lightweight and flexible, which is important for many applications. The output power of a-Si PV products also has a positive temperature coefficient: at higher ambient temperature, e.g., in areas with more sunshine, the efficiency is higher.

Compared with other types of thin film PV technologies, such as CdTe and copper-indium-diselenide (CIS) based PV technologies which have demonstrated higher efficiency in small-area R&D type cells, a-Si photovoltaics looks attractive because (i) it has been developed for approximately twenty years and the production process is more mature and proven; and (ii) the product does not contain any hazardous materials such as Cadmium as in CdTe photovoltaics or a large amount of expensive metal such as indium as in CIS-based photovoltaics. The materials in amorphous silicon based cells originate in raw materials that are abundant on earth.

### *7.2 Critical Issues for Further Enhancement and Future Potential*

To increase application of a-Si based PV significantly beyond today's level, the following issues are critical and must be addressed.

1. Light-induced degradation must be better understood. Approaches for reducing or controlling the degradation need to be further developed. At this moment, there are

many engineering compromises in the device design, such as the use of thin i-layers to limit the degradation. If the materials can be made more stable under light, these compromises can be relaxed and the device can be made with much higher efficiency.

2. As the gross defects associated with light-soaking are minimized, we shall need to explore improvements in the drift mobility of holes.
3. We need to improve a-SiGe so that narrower bandgap materials can be incorporated into cells and more of the infrared region of the solar spectrum can be exploited.
4. Faster deposition processes need to be developed that (at least) preserve the conversion efficiencies achieved by present processes. This is critical for low-cost and high-throughput manufacturing. In addition, these high-rate processes must also achieve high gas utilization.
5. Microcrystalline Si based solar cells need to be fully explored as alternative, narrow bandgap component cells in tandem or triple junction cells. We expect that rather fast, >2 nm/s, deposition processes will be required. The device physics of μc-Si based solar cells, especially the possibilities for improving the open circuit voltage, need to be better understood.
6. Module design needs to be further improved, and the costs associated with framing and encapsulation need to be further reduced. At the same time the durability of modules in standard environmental tests must be preserved or improved.
7. We need to find new applications for a-Si PV products in all of its present markets, including building-integrated PV, space power, and consumer electronics as well as grid-connected, large-scale power generation.

As these critical issues are successfully addressed, we expect that a-Si based solar cells will become more inexpensive, that there will be explosive increases in the volume of production and widespread expansion in the market. Amorphous silicon based cells will become an environmentally friendly, inexpensive, and ubiquitous source of electrical power for our life on Earth!

## Acknowledgments

This work was supported by the Thin Film Photovoltaics Partnership of the U.S. National Renewable Energy Laboratory. We thank Rana Biswas (Iowa State University), Nerio Cereghetti (LEEE), Gautam Ganguly (BP Solar, Inc.), Subhendu Guha (United Solar Systems Corp.), Scott Jones (Energy Conversion Devices), Stan Ovshinsky (Energy Conversion Devices), Bolko von Roedern (National Renewable Energy Laboratory), Chris Wronski (Pennsylvania State University), and Jeff Yang (United Solar Systems Corp.) for their generous help in writing this article.

---

1 Williams E M, *The Physics and Technology of Xerographic Processes*, Wiley, New York, (1984).
2 Mort J, *The Anatomy of Xerography: Its Invention and Evolution,* McFarland, Jefferson, N.C. (1989).
3 An historical discussion is given by Chittick R C and Sterling H F, in *Tetrahedrally Bonded Amorphous Semiconductors*, edited by Adler D and Fritzsche H, Plenum, New York (1985), 1.
4 Spear W E and LeComber P G, *Solid State Comm.* **17**, 1193 (1975).
5 Carlson D E and Wronski C R, *Appl Phys. Lett.* **28**, 671 (1976).
6 Perlin J, *Space to Earth: The Story of Solar Electricity* (aatec publications, Ann Arbor, 1999).
7 Wronski C R and Carlson D E, in *Clean Electricity from Photovoltaics*, edited by Archer M D and Hill R, World Scientific (2001).
8 Yang J, Banerjee A, and Guha S, *Appl. Phys. Lett.* **70**, 2977 (1997).
9 Fritzsche H, in *Amorphous and Heterogeneous Silicon Thin Films*, p. A17.1, edited by Collins R W, *et al.,* Materials Research Society, Symposium Proceedings Vol. 609, Warrendale (2001), A17.1.
10 Vaněček M A, Poruba A, Remeš Z, Beck N, and Nesládek M, *J. Non-Cryst. Solids* **227-230**, 967 (1998).
11 The figure was calculated based on the hemispherical irradiance (37° south facing) American Society for Testing and Materials (ASTM) Table G159-98 Standard Tables for References Solar Spectral Irradiance at Air Mass 1.5: Direct Normal and Hemispherical for a 37° Tilted Surface.
12 Near room temperature, a-Si:H has a "quantum efficiency" of essentially 1.00 for generating photocarriers when a photon is absorbed. Carasco F and Spear W E, *Phil. Mag. B* **47**, 495 (1983). This ideal value is rather surprising. Many other non-crystalline materials have "geminate recombination" of the electron and hole immediately after their generation, which would of course lead to a loss of conversion efficiency; see ref. 13.
13 Schiff E A, *J. Non-Cryst. Solids***190**, 1 (1995).
14 Guha S, in *Technology and Applications of Amorphous Silicon*, 252-305, edited by Street R A, Springer, Berlin (1999). Fig. 6.10 of this paper is a valuable compilation of power measurements for varying cell thicknesses and light-soaking histories.
15 Guha S, Yang J, Banerjee A, Glatfelter T, Hoffman K, Xu X, *Technical Digest - 7th International Photovoltaic Science and Engineering Conference, Nagoya, Japan (PVSEC-7)*, p. 43 (1993).
16 Staebler D L and Wronski C R, *Appl. Phys. Lett.***31**, 292 (1977).
17 Shugar D., in *Proceedings of the 24th Photovoltaic Specialists Conference*, 670 IEEE (1994).
18 Emery K, Burdick J, Calyem Y, Dunlavy D, Field H, Kroposki B, Moriary T, Ottoson L, Rummel S, Strand T, and Wanlass M W, in *Proceedings of the 25th Photovoltaic Specialists Conference,* 1275, IEEE (1996).
19 Kameda M, Sakai S, Isomura M, Sayama K, Hishikawa Y, Matsumi S, Haku H, Wakisaka K, Tanaka K, Kiyama S, Tsuda S, and Nakano S, in *Proceedings of the 25th Photovoltaic Specialists Conference,* 1049, IEEE (1996).
20 del Cueto J A and von Roedern B, *Prog. Photovolt: Res. Appl.* **7**, 101 (1999).
21 Carlson D E, Lin G, and Ganguly G, in *Proceedings of the 28th Photovoltaic Specialists Conference,* 707, IEEE (2000).
22 Measurements furnished through the courtesy of N. Cereghetti, Laboratory of Energy, Ecology and Economy (LEEE), Scuola Universitaria Professionale della Svizzera Italiana. These data apply to the 0.5 kW array, and are described in more detail by Cereghetti N, Chianese D, Rezzonico S, and

Travaglini G, in *Proceedings of the 16th European Photovoltaic Solar Energy Conference,* James and James, London (2001).
23 Street R A, *Hydrogenated Amorphous Silicon,* Cambridge University Press, Cambridge (1991).
24 Phillips J C, *J. Non-Cryst. Solids* **34**, 153 (1979).
25 Boolchand P and Thorpe M F, *Phys. Rev. B* 50, 10366 (1994).
26 Reimer J A and Petrich M A, in *Amorphous Silicon and Related Materials, Vol. A*, 3, edited by Fritzsche H, World Scientific, Singapore (1989).
27 Zhao Y, Zhang D L, Kong G L, Pan G, and Liao X B, *Phys. Rev. Lett*. **74**, 558 (1995).
28 Santos P V, Johnson N M, and Street R A, *Phys. Rev. Lett.* **67**, 2686 (1991).
29 Beyer W, Herion J, Wagner H, and Zastrow U, *Phil. Mag.* **B63**, 269 (1991).
30 Figure courtesy of R. Biswas; for information on the calculations, see Biswas R and Li Y P, *Phys. Rev. Lett.* 82, 2512 (1999).
31 The assignment of the D-center observed in electron paramagnetic resonance measurements with a dangling bond has been challenged in favor of "floating bonds" (Stathis J H and Pantelides S T, *Phys. Rev. B* **37**, 6579-6582 (1988)).
32 Zafar S and Schiff E A, *Phys. Rev. Lett*. **66**, 1493 (1991).
33 Jackson W B, Tsai C C, and Thompson R, *Phys. Rev. Lett.* **64**, 56 (1990).
34 Park H R, Liu J Z, and Wagner S, *Appl. Phys. Lett.* **55**, 2658 (1989).
35 See the review of Fritzsche H, *Annu. Rev. of Mater. Res.* **31**, 47 (2001).
36 Branz H M, *Phys. Rev. B* **59**, 5498 (1999).
37 Ley L, *J. Non-Cryst. Solids* **114**, 238 (1989).
38 Jackson W B, Kelso S M, Tsai C C, Allen J W, and Oh S J, *Phys. Rev. B* **31**, 5187 (1985).
39 Cody G, Tiedje T, Abeles B, Brooks B, and Goldstein Y, *Phys. Rev. Lett.* **47**, 1480 (1981).
40 Tiedje T, in *Hydrogenated Amorphous Silicon II*, 261-300, edited by Joannopoulos J D and Lucovsky G, Springer-Verlag, New York (1984).
41 Gu Q, Wang Q, Schiff E A, Li Y-M, and Malone C T, *J. Appl. Phys.* **76**, 2310 (1994).
42 Wang Q, Antoniadis H, Schiff E A, and Guha S, *Phys. Rev. B* **47**, 9435 (1993).
43 Gu Q, Schiff E A, Chevrier J-B, and Equer B, *Phys. Rev. B* **52**, 5695 (1995).
44 Mott N V, *Conduction in Non-Crystalline Solids,* Oxford University Press, Oxford (1987).
45 Tauc J, in *Optical Properties of Solids*, 277, ed. Abeles F, North Holland, Amsterdam (1972).
46 Chen I S and Wronski C R, *J. Non-Cryst. Solids* **190**, 58 (1995).
47 Jackson W B and Amer N, *Phys. Rev. B* **25**, 5559 (1982).
48 Lee J-K and Schiff E A, *Phys. Rev. Lett.* **68**, 2972 (1992)
49 Antoniadis H and Schiff E A, *Phys. Rev. B* **46**, 9482--9492 (1992)
50 Han D, Melcher D C, Schiff E A, and Silver M, *Phys. Rev. B* **48**, 8658 (1993).
51 Hama S T, Okamoto H, Hamakawa Y, and Matsubara T, *J. Non-Cryst. Solids* **59-60**, 333 (1983).
52 Guha S, Payson J S, Agarwal S C, Ovshinsky S R, *J. Non-Cryst. Solids* **97&98**, 1455 (1987).
53 Middya A R, Ray S, Jones S J, and Williamson D L, *J.Appl. Phys.* **78**, 4966 (1995).
54 Stutzmann M, Street R A, Tsai C C, Boyce J B, and Ready S E, *J. Appl. Phys.* **66**, 569 (1989).
55 Li Y-M, Catalano A, and Fieselmann B F, in *Amorphous Silicon Technology – 1992*, edited by Thompson M J *et al.*, 923, Materials Research Society, Symposium Proceedings Vol. 258, Pittsburgh (1993).
56 Arya R R, Catalano A, and Oswald R S, *Appl. Phys. Lett.* **49**, 1089 (1986).
57 Tsukada T, in *Technology and Applications of Amorphous Silicon,* 7, edited by Street R A, Springer, Berlin (2000).
58 Chittick R, Alexander J, Sterling H, J. Electrochem. Soc. **116**, 77-81 (1969).
59 Spear W E, LeComber P G, *J. Non-Cryst. Solids* **8-10**, 727-738 (1972).
60 Chapman B, *Glow Discharge Processes*, John Wiley & Sons, New York, NY (1980).
61 Luft W, Tsuo Y, *Hydrogenated Amorphous Silicon Alloy Deposition Processes*, Marcel Dekker, Inc, New York, NY (1993).
62 Guha S, Yang J, Banerjee A, Glatfelter T, Hoffman K, Ovshinsky S, Izu M, Ovshinsky H, Deng X, *Materials Research Society Symp. Proc. Vol.* **336**, 645 (1994).

63 Arya R, Carlson D, *Progress in Photovoltaics: Research and Applications* **10**, 2002. pp69-76.
64 Carlson D, US Patent 4,317,844, issued March 2, 1982.
65 Curtins H, Wyrsch N, Shah A, *Electronics Lett.* **23**, 228-230 (1987).
66 Chatham H, Bhat P, Benson A, Matovich C, *J. Non-Cryst. Solids* **115**, 201-203 (1989).
67 Saito K, Sano M, Matsuyama J, Higasikawa M, Ogawa K, Kajita I, *Tech. Digest PVSEC-9*, 579 (1996).
68 Matsumura H, *Jpn. J. Appl. Phys.* **25**, L949-951 (1986).
69 Mahan A, Carapella J, Nelson B, Crandall R, Balberg I, *J. Appl . Phys*. **69**, 6728-6730 (1991).
70 Konagai M, Kim W, Tasaki H, Hallerdt M, Takahashi K, *AIP Conf. Proc. 157*, 142-149 (1987).
71 Rocheleau R, Hegedus S, Buchanan W, Jackson S, *Appl. Phys. Lett.* **51**, 133-135 (1987).
72 Paul W, Lewis A, Connel G, Moustakas T, *Solid State Comm.* **20**, 969-972 (1976).
73 Moustakas T, Wronski C, Tiedje T, *Appl. Phys. Lett.* **39**, 721-723 (1981).
74 Knights J, *Materials Research Society Symp. Proc. Vol.* **38**, 372 (1985).
75 Ueda M, Imura T, Osaka Y, in *Proc. 10th Symp. on Ion Sources and Ion-Assisted Technology,* (1986).
76 Deng X, Narasimhan K, Evans J, Izu M, Ovshinsky S, *Proc. 1st World Conf. on Photovoltaic Energy Conversion*, 678 (1994).
77 Yang J, Xu X, Banerjee A, Guha S, *Proceedings of the 25th Photovoltaic Specialists Conference*, 1041 (1996).
78 Cherepin V, *Secondary Ion Mass Spectroscopy of Solid Surfaces*, published by Coronet Books, Dec. 1987.
79 Kampas F , *J. Appl. Phys.* **54**, 2276-2280 (1983).
80 Jasinski, JM, Whittaker, EA, Bjorklunk GC, Dreyfus RW, Estes RD and Walkup RE., *Appl. Phys. Lett.* **44**, 1155-1157 (1984).
81 Robertson R, Gallagher A., *J. Chem. Phys.* **85**, 3623-3630 (1986).
82 Gallagher A, *J. Appl. Phys.* **63**, 2406-2413 (1988
83 Shah A, Dutta J, Wyrsch N, Prasad K, Curtins H, Finger F, Howling A, Hollenstein C, *Materials Research Society Symp. Proc. Vol.* **258**, 15 (1992).
84 Heintze M, Zedlitz R, Bauer G, *Materials Research Society Symp. Proc. Vol.* **297**, 49-54 (1993).
85 Deng X, Jones S, Liu T, Izu M, Ovshinsky S, *Proceedings of the 26th Photovoltaic Specialists Conference*, 591 (1997).
86 Ito N, Kondo M, Matsuda A, *Proceedings of the 28th Photovoltaic Specialists Conference*, 900 (2000).
87 Kato I, Wakana S, Hara S, and Kezuka H, *Jpn. J. Appl. Phys.* **21**, L470 (1982)
88 Hudges S, Johncock A, and Ovshinsky S, *J. Non-Crystal. Solids* **77&78**, 809 (1985).
89 Watanabe T, Azuma K, Nakatani M, Suzuki K, Sonobe T, Shimada T, *Jpn, J. Appl. Phys.* **25**, 1805 (1986).
90 Guha S, Xu X, Yang J, Banerjee A, *Materials Research Society Symp. Proc. Vol.* **377**, 621-626 (1995).
91 Saito K, Sano M, Ogawa K, Kajita I, *J. Non-Cryst. Solids* **164-166**, 689 (1993).
92 Saito K, Sano M, Matsuyama J, Higasikawa M, Ogawa K, Kajita I, *Tech. Digest PVSEC-9*, 579 (1996).
93 Wiesmann H, Ghosh A, McMahon T, and Strongin M, *J. Appl. Phys.* **50**, 3752 (1979).
94 Wang Q, Iwaniczko E, Yang J, Lord K, Guha S, Wang K, Han D, *Proceedings of the 29th Photovoltaic Specialists Conference*, (2002).
95 Mahan A, Xu Y, Iwaniczko E, Willliamson D, Nelson B, Wang Q, *J. Non-Cryst. Solids* **299-302**, 2-8 (2002).
96 Mahan A, Xu Y, Nelson B, Crandall R, Cohen J, Palinginis K, Gallagher A, *Appl. Phys. Lett.* **78**, 3788 (2001).
97 Povolny H, Deng X, to be published in *Proc. 2nd Int. Conf. on Cat-CVD (HW CVD) Processes* (2002).
98 Morrison S, Madan A, *Proceedings of the 28th Photovoltaic Specialists Conference*, 837 (2000).
99 Moustakas T, Maruska H, Friedman R, *J. Appl. Phys.* **58**, 983-986 (1985).

100 Abelson J, Doyle J, Mandrell L, Maley N, *Materials Research Society Symp. Proc. Vol.* 268, 83-94 (1992).
101 Miller D, Lutz H, Weismann H, Rock E, Ghosh A, Ramamoorthy S, Strongin M, *J. Appl. Phys.* **49**, 6192-6193 (1978).
102 Shimizu T, Kumeda M, Morimoto A, Tsujimura Y, Kobayashi I, *Materials Research Society Symp. Proc. Vol.* **70**, 311-318 (1986).
103 Hanna J, Kamo A, Azuma M, Shibata N, Shirai H, Shimizu I, *Materials Research Society Symp. Proc. Vol.* **118**, 79-84 (1988).
104 Parsons G, Tsu D, Lucovsky G, *J. Vac. Sci. Technol. A* **6**, 1912-1916 (1988).
105 Sakamoto Y, *Jpn. J. Appl. Phys.* **16**, 1993-1998 (1977).
106 Dalal V, Maxson T, Girvan R, Haroon S, *Materials Research Society Symp. Proc. Vol.* **467**, 813-817 (1997).
107 Hanabusa M, Suzuki M, *Appl. Phys. Lett.* **39**, 431-432 (1981).
108 Ovshinsky S, Deng X, Young R, US Patent 5,231,047 (1993).
109 Jones S, Crucet R, Deng X, Izu M, *Materials Research Society Symp. Proc. Vol.* **609**, A4.5 (2000).
110 Guha S, Narasimhan K, Pietruszko S, *J. Appl. Phys.* **52**, 859 (1981).
111 Tanaka K, Matsuda A, *Materials Science Reports* **2**, 139-184 (1987).
112 Yang J, Lord K, Guha S, Ovshinsky S, *Materials Research Society Symp. Proc. Vol.* **609**, A15.4 (2000).
113 Yang J, Xu X, Guha S, *Materials Research Society Symp. Proc. Vol.* **336**, 687-692 (1994).
114 Yang L, Chen L, *Materials Research Society Symp. Proc. Vol.* 336, 669-674 (1994).
115 Ferlauto A, Koval R, Wronski C, Collins R, *Appl. Phys. Lett.* **80**, 2666 (2002).
116 Yang J, Banerjee A, Lord K, Guha S, Proc. 28th IEEE PVSC, 742 (2000).
117 Deng X, in Record of the NREL-EPRI Amorphous Silicon Guidance Team Review Meeting, February 25-26, 2002.
118 Deng X, Narasimhan K, Evans J, Izu M, Ovshinsky S, *Proc. 1st World Conf. PVSEC*, 678 (1994).
119 Deng X, Annual Subcontract Report, submitted to NREL, NREL/TP-411-20687. Feb. 1996. "Development of high, stable-efficiency triple-junction a-Si alloy solar cells".
120 Ovshinsky S, Guha S, Yang C, Deng X, Jones S, US Patent 8,766,219 (1996).
121 Liao X, Wang W, Deng X, *Proceedings of the 29th Photovoltaic Specialists Conference* (2002).
122 Koval R, Chen C, Gerreira G, Ferlauto A, Pearce J, Rovira P, Collins R, Wronski C, *Proceedings of the 29th Photovoltaic Specialists Conference* (2002).
123 AMPS-1D is a copyright of Pennsylvania State University. Zhu H and Fonash S, in *Amorphous and Microcrystalline Silicon Technology – 1998*, 395, edited by Schropp R E I, *et al.,* Materials Research Society, Symp. Proc. Vol 507, Pittsburgh, 1998).
124 Schropp R E I and Zeman M, *Amorphous and Microcrystalline Silicon Solar Cells: Modeling Materials, and Device Technology*, Kluwer, Boston (1998).
125 Welcome, expert. The electronic characteristics of a-Si:H used in the modeling in this chapter include only bandtail states – and not defects. The parameters for a-Si:H are published in Jiang L, Rane S, Schiff E A, Wang Q, Yuan Q, in *Amorphous and Heterogeneous Films – 2000*, A18.3.1-11, edited by Branz H M, *et al.* (Materials Research Society, Symp. Proc. Vol. 609, Pittsburgh, 2001).
126 $K = \{\sin(\alpha\pi)\}/\{\alpha(1-\alpha)\pi\}$.
127 Scher H, Shlesinger M F, and Bendler J T, *Physics Today* **44** (1), 26 (1991).
128 Crandall R S, *J. Appl. Phys.* **54**, 7176 (1983).
129 Hegedus S, *Prog. Photovolt. Res. Appl.* **5**, 151 (1997).
130 Crandall R S and Schiff E A, in *13th NREL Photovoltaics Program Review,* 101—106, edited by Ullal H S and Witt C E, Amer. Inst. of Phys., Conf. Proc. Vol. 353, Woodbury (1996).
131 Pearce J M, Koval R J, Ferlauto A S, Collins R W, Wronski C R, Yang J, and Guha S, *Appl. Phys. Lett.* **77**, 19 (2000).
132 Rose A, *Photoconductivity and Allied Phenomena* (Krieger, 1978).
133 Fonash S, *Solar Cell Device Physics* (Wiley, 1981).

134 Tiedje T, *Appl. Phys. Lett.* **40**, 627 (1982).
135 Guha S, Yang J, Nath P, and Hack M, *Appl. Phys. Lett.* **49**, 218 (1986).
136 Arya R R, Catalano A, and Oswald R S, *Appl. Phys. Lett.* **49**, 1089 (1986).
137 Hegedus S S, Rocheleau R E, Tullman R N, Albright D E, Saxena N, Buchanan W A, Schubert K E, and Dozler R, in *Conference Record of the 20th IEEE Photovoltaic Specialists Conference,* 129 Institute of Electrical and Electronics Engineers (1988).
138 Sakai H, Yoshida T, Fujikake S, Hama T, and Ichikawa Y, *J. Appl. Phys.* **67**, 3494 (1990).
139 Yablonovitch E, *J. Opt. Soc. Am.* **72**, 899 (1982).
140 Deckman H W, Wronski C R, Witzke H, and Yablonovitch E, *Appl. Phys. Lett.* **42**, 968 (1983).
141 Hegedus S and Deng X, *Conference Record of the 25th IEEE Photovoltaic Specialists Conference,* 1061, Institute of Electrical and Electronics Engineers (1996).
142 Hegedus S, Buchanan W, Liu X, and Gordon R, *Conference Record of the 25th IEEE Photovoltaic Specialists Conference,* 1129, Institute of Electrical and Electronics Engineers (1996).
143 Lechner P, Geyer R, Schade H, Rech B, and Müller J, *Conference Record of the 28th IEEE Photovoltaic Specialists Conference,* 861, Institute of Electrical and Electronics Engineers (2000).
144 Banerjee A and Guha S, *J. Appl. Phys.* **69**, 1030 (1991).
145 Sze S, *Physics of Semiconductor Devices*, 798, John Wiley & Sons, New York, NY (1981)
146 Mitchell C et al, *Proc. 7th PVARD Program Review Meeting* (1984).
147 Kuwano Y, et al., *Conference Record of the 16th IEEE Photovoltaic Specialists Conference*, 1338, Institute of Electrical and Electronics Engineers (1982).
148 The thickness of i-layers are in the range of 100nm to 200nm, while for single junction a-Si solar cells the i-layer needs to be much thicker to get high efficiency.
149 Hack M, Shur M, J. Appl. Phys. 59, 2222 (1986).
150 Agarwal P, Povolny H, Han S, Deng X, ##,*J. Non-Cryst. Solids* (2002).
151 Yang L, Chen L, Catalano A, *Materials Research Society Symp. Proc. Vol.* **219**, 259-264 (1991).
152 Guha S, Yang J, Pawlikiewicz A, Glatfelter T, Ross R, Ovshinsky S, *Appl. Phys. Lett.* **54**, 2330 (1989).
153 Zimmer J, Stiebig H, Wagner H, *J. Appl. Phys.* **84**, 611-617 (1998).
154 Yang J, Banerjii, A, Glatfelter T, Sugiyama S, Guha S, *Conference Record of the 26th IEEE Photovoltaic Specialists Conference,* 563, Institute of Electrical and Electronics Engineers (1997).
155 Hamakawa Y, Tawada Y, Nishimura K, Tsuge K, Kondo M, Fujimoto K, Nonomura S, Okamoto H, *Conference Record of the 16th IEEE Photovoltaic Specialists Conference*, 679-684, Institute of Electrical and Electronics Engineers (1982).
156 Guha S, in Technology and Applications of Amorphous Silicon, ed. R.A. Street, published by Springer-Verlag Berlin Heidelberg New York, 2000. (See Table 6.9 in the reference)
157 Iida H, Shiba N, Mishuka T, Karasawa H, Ito A, Yamanaka M, Hayashi Y, *IEEE Electron Dev. Lett.* **EDL-4**, 157-159 (1983).
158 Gordon R, Proscia J, Ellis F, Delahoy A, *Solar Energy Mater.* **18**, 263-281 (1989).
159 Hegedus S, Kampas F, Xi J, *Appl, Phys. Lett.* **67**, 813 (1995).
160 See Chapter ?? of this Handbook on IV measurements.
161 Yoshida T, Tabuchi K, Takano A, Tanda M, Sasaki T, Sato H, Fijikake S, Ichikawa Y, Harashima K, *Conference Record of the 28th IEEE Photovoltaic Specialists Conference*, 762-765 (2000).
162 Wang W, Povolny H, Du W, Liao X, Deng X, *Conference Record of the 29th IEEE Photovoltaic Specialists Conference*, *in press* (2002).
163 Nomoto K, Saitoh H, Chida A, Sannomiya H, Itoh M, Yamamoto Y, in *Intl. Tech. Digest PVSEC-7*, 275 (1993).
164 Arya R, Oswald R, Li Y, Maley N, Jansen K, Yang L, Chen L, Willing F, Bennett M, Morris J, Carlson D, *Proc. of First WCPEC*, 394 (1994).
165 Hishikawa Y, Ninomiya K, Maryyama E, Kuroda S, Terakawa A, Sayama K, Tarui H, Sasaki M, Tsuda S, Nakano S, *Proc. 1st WCPEC*, 386-393 (1994).
166 Meier J, Keppner H, Dubail S, Droll U, Torres P, Pernet P, Ziegler Y, Selvan J, Cuperus J, Fischer D, Shah A, *Materials Research Society Symp. Proc. Vol.* 507, pp ## (1998).

167 Saito K, Sano M, Matuda K, Kondo Takaharu, Nishimoto T, Ogawa K, Kajita I, *Proc. 2nd WCPEC*, 351-354 (1998).
168 Yamamoto K, Yoshimi M, Suzuki T, Okamoto Y, Tawada Y, Nakajima A, *Conference Record of the 26th IEEE Photovoltaic Specialists Conference*, 575-580 (1997).
169 Jones S, Crucet R, Capangpangan R, Izu M, Banerjee A, *Materials Research Society Symp. Proc. Vol.* 664, A15.1 (2001).
170 Burdick J, Glatfelter T, *Solar Cells*, **18**, 310-314 (1986).
171 Mueller R, *Solar Energy Materials and Solar Cells* **30**, 37-45 (1993).
172 Veprek S, Marecek V, *Solid St. Electr.* **11**, 683 (1968).
173 Hattori Y, Kruangam D, Toyama T, Okamoto H, Hamakawa Y, *Tech. Digest PVSEC-3*, 171 (1987).
174 Faraji M, Gokhale S, Ghoudhari S, Takwake M, Ghaisas S, *Appl. Phys. Lett.* **60**, 3289-3291 (1992).
175 Meier J, Fluckiger R, Keppner H, Shah A, *Appl. Phys. Lett.* **65** 860-862 (1994).
176 Meier J, Kroll U, Dubail S, Golay S, Fay S, Dubail J, Shah A, *Conference Record of the 28th IEEE Photovoltaic Specialists Conference*, 746-749 (2000). .
177 Yamamoto K, *Materials Research Society Symp. Proc. Vol.* **507**, pp ## (1998).
178 Repmann T, Appenzeller W, Roschek T, Rech B, Wagner H, *Conference Record of the 28th IEEE Photovoltaic Specialists Conference,* 912-915 (2000).
179 Rath J, Galetto M, van der Werf C, Feenstra K, Meiling H, van Cleef M, Schropp R, *Tech. Dig. 9th Int. PV Sci. and Eng. Conf* 227 (1996).
180 Jones S, Crucet R, Deng X, Izu M, *Materials Research Society Symp. Proc. Vol.* **609**, A4.5 (2000).
181 Roschek, Repmann T, Muller J, Rech B, Wagner H, *Conference Record of the 28th IEEE Photovoltaic Specialists Conference-1996*, 150-153 (2000).
182 Meier J, Dubail S, Cuperus J, Kroll U, Platz R, Torres P, AnnaSelvan J, Pernet P, Pellaton N, Fischer D, Keppner H, Shah A, *J. Non-Cryst. Solids* **227-230**, 1250 (1998).
183 Platz R, Pellaton Vaucher N, Fischer D, Meier J, Shah A, *Conference Record of the 26th IEEE Photovoltaic Specialists Conference*, 691-694 (1997).
184 Shah A, Meier J, Vallat-Sauvain E, Droz C, Kroll U, Wyrsch N, Guillet J, Graf U, *Thin Solid Films* **403-404**, 179-187 (2002).
185 Izu M, Ovshinsky S, *Thin Solid Films* **119**, 55 (1984).
186 Izu M, Deng X, Krisko A, Whelan K, Young R, Ovshinsky H, Narasimhan K, Ovshinsky S, *Conference Record of the 23th IEEE Photovoltaic Specialists Conference*, 919 (1993).
187 Guha S, Yang J, Banerjee A, Glatfelter T, Hoffman K, Ovshinsky S, Izu M, Ovshinsky H, Deng X, *Materials Research Society Symp. Proc. Vol.* **336**, 645 (1994).
188 Deng X, Narasimhan K. *IEEE 1st World Conf. on Photovoltaic Energy Conversion*, 555 (1994).
189 Nath P, Hoffman K, Vogeli C, Ovshinsky S, *Appl. Phys. Lett.* **53**, 986-988 (1988).
190 Frammelsberger W, Lechner P, Rubel H, Schade H, *Proc. 14th European Photovoltaic Solar Energy Conference*, 2006 (1997).
191 Forest H, *Proc. 14th European Photovoltaics Solar Energy Conf.*, 2018-2020 (1997).
192 Rech B *et al*., *Proc. 2nd World Conf. on Photovoltaic Solar Energy Conversion*, 391-396 (1998).
193 Kinoshita T, *et al.*, *Proc. 14th EU PVSEC*, 566 (1997).
194 Okamoto S, Terakawa A, Maruyama E, Shinohara W, Hishikawa Y, Kiyama S, *Conference Record of the 28th IEEE Photovoltaic Specialists Conference*, 736-741 (2000).
195 Yamamoto K, Yoshimi M, Suzuki T, Nakata T, Swada T, Nakajima A, Hayashi K, *Conference Record of the 28th IEEE Photovoltaic Specialists Conference,* 1428-1432 (2000).
196 Hagedorn G, *Proc. 9th European PVSEC*, Freiburg, 542 (1989).